ELSEVIER

Available online at www.sciencedirect.com

SCIENCE DIRECT®

Journal of Computational Physics 188 (2003) 640–677

JOURNAL OF COMPUTATIONAL PHYSICS

www.elsevier.com/locate/jcp

Surface evolution in bare bamboo-type metal lines under diffusion and electric field effects

Amir Averbuch [a,*], Moshe Israeli [b], Menachem Nathan [c], Igor Ravve [d]

[a] *Department of Computer Science, School of Computer Science, Tel Aviv University, Tel Aviv 69978, Israel*
[b] *Faculty of Computer Science Technion, Haifa 32000, Israel*
[c] *Department of Electrical Engineering-Physical Electronics, Tel Aviv University, Tel Aviv 69978, Israel*
[d] *Computing Science Department, Lawrence Berkeley Lab, University of California, USA*

Received 24 May 2002; received in revised form 18 March 2003; accepted 19 March 2003

Abstract

Irregularities such as voids and cracks often occur in bamboo-type metal lines of microelectronic interconnects. They increase the resistance of the circuits, and may even lead to a fatal failure. In this work, we analyze numerically the electromigration of an unpassivated bamboo-type line with pre-existing irregularities in its top surface (also called a grain–void interface). The bamboo line is subjected to surface diffusion forces and external electric fields. Under these forces, initial defects may either heal or become worse. The grain–void interface is considered to be one-dimensional, and the physical formulation of an electromigration and diffusion model results in two coupled, fourth order, one-dimensional time-dependent PDEs, with the boundary conditions imposed at the electrode points and at the triple point, which belongs to two neighboring grains and the void. These equations are discretized by finite differences on a regular grid in space, and by a Runge–Kutta integration scheme in time, and solved simultaneously with a static Laplace equation describing the voltage distribution throughout each grain, when the substrate conductivity is neglected. Since the voltage distribution is required only along an interface line, the two-dimensional discretization of the grain interior is not needed, and the static problem is solved by the boundary element method at each time step. The motion of the interface line is studied for different ratios between diffusion and electric field forces, and for different initial configurations of the grain–void interface. We study plain and tilted contour lines, considering positive and negative tilts with respect to the external electric field, a stepped contour with field lines entering or exiting the 'step', and a number of modifications of the classical Mullins problem of thermal grooving. We also consider a two-grain Mullins problem with a normal and tilted boundary between the grains, examining positive and negative tilts.
© 2003 Elsevier Science B.V. All rights reserved.

1. Introduction

In this paper, we develop a numerical approach for tracking the dynamics of a grain–void interface under the action of diffusion forces and an external voltage. Consider a curved line, which separates a grain

* Corresponding author. Tel.: +972-3-640-2020; fax: +972-3-640-9357.
E-mail address: amir@math.tau.ac.il (A. Averbuch).

0021-9991/03/$ - see front matter © 2003 Elsevier Science B.V. All rights reserved.
doi:10.1016/S0021-9991(03)00199-2

from the void. The basic assumption is that the interface moves in its normal direction with a known speed function F. The tangential motion is usually neglected when a void inside a single grain is considered. For an intergranular void, the tangential motion is allowed along with the normal motion in the proximity of a triple point, which belongs to each of two grains and to the void, otherwise the boundary conditions cannot be satisfied. The front velocity includes surface diffusion and electromigration components, which depend on the second derivatives of the interface curvature K and of the voltage U, respectively [2,3]. The derivatives are taken with respect to the interface arclength s

$$F = BK_{ss} + \alpha U_{ss}. \tag{1}$$

Positive coefficients B and α express the contribution of the diffusion forces and the field forces, respectively. They depend on the properties of the material, temperature, etc., and are considered constant. Normalizing the physical time of the problem $\tau = Bt$, one can assume $B = 1$ without any loss of generality.

The analysis does not take into account surface diffusional anisotropy. In this study, we do not consider the action of the mechanical stresses that takes place in the metal lines due to their encapsulation by dielectric materials.

2. Electromigration in thin films: review

Predictions for dynamics and evolution of voids and cracks in thin metallic films of interconnect lines have a practical importance for microelectronics technology, and many researchers have contributed to this field. In this section we review the most relevant prior art. Xia et al. [9] introduced a two-dimensional finite element method to compute the motion and evolution of a void in a single grain by surface diffusion in an elastic, electrically conductive solid. They accounted for the influence of deformation, electric current flow, and effects of mass flow. The methodology was used to predict the conditions of failure of the interconnect. A three-dimensional finite element model for studying the motion and evolution of voids in an idealized interconnect line due to electromigration and strain-induced surface diffusion was developed by Zhang et al. [10] to predict more accurately the behavior of a void. The spatial finite element formulation was further exploited by Zhang and Bower [11] to study the conditions for formation of islands in a thin film of semiconductor material. Kraft et al. [12] presented the results of experimental studies of the mechanical behavior of thin films. Films on the silicon and polymer substrates were strained, and the film stress was determined by X-ray measurements.

Kraft and Arzt [21] examined electromigration mechanisms in conductor lines, applying finite difference and finite element formulations, and compared the results of numerical simulations with experimental studies. They analyzed electromigration damage in unpassivated aluminum-based interconnect lines, and discovered that slit-like voids in bamboo lines develop from equiaxed voids through a shape change driven by the "electron wind", taking into account the finite width of the line, surface tension effects, and anisotropic diffusivity. Further, Kraft and Arzt [23] developed a model to predict lifetimes of conductor lines and to describe the microscopic damage behavior, considering nucleation and growth of electromigration voids. They found that the reliability of a bamboo line is governed by the critical current density.

Experimental and theoretical studies of aluminum interconnects that include copper as an alloying element were carried out by Spolenak et al. [22]. A mechanistic model was developed to account for an increase in activation energies for aluminum drift in alloys in comparison to the pure metal, and this approach yielded results in good agreement with the experiments. Copper as an alloying element improves strongly the electromigration resistance of the interconnects, and thus reduces the damage caused by evolution and growth of voids.

Gungor and Maroudas in a series of papers [13,14,24,27,32–34] and with collaborators [26] studied the complex problem of linear and non-linear dynamics and stability of transgranular voids in thin films with bamboo grain structure. In [13] they simulated the formation of various morphological features: void faceting, formation of wedge-shaped voids, propagation of slit-like and soliton-like features, and open-circuit failures. Since the electric field distribution is needed only on the void surface, the distribution of electric field was computed by the boundary element method (BEM), with the use of the Galerkin scheme and linear trial functions. Integration of the governing equation was carried out with a variable time step, which was determined according to the maximum computed normal velocity of the grain–void interface and the minimum BEM grid size on the void surface. This leads to a small time step and to negligible perturbations in the distribution of the electric field within each such time period. The electric field need not be calculated after every single time step. In this study, Gungor and Maroudas applied the variable frequency of updating the electric field distribution. This frequency is high where the proximity of the top of the void surface to the top edge of the film results in significant current crowding. In [14] they performed a theoretical analysis for conditions of failure of metallic films. The dynamics of voiding is governed by surface mass transport, electric fields, and elastic and plastic deformations. Anisotropic properties were taken into account in surface diffusivity and stresses. In [34] they applied a linear stability theory to examine the effects of anisotropy in surface diffusion. In [33] they performed a theoretical analysis and numerical simulations of the effects of residual stress on the failure mechanisms of passivated metallic thin films, and observed two modes of failure to occur concurrently during void morphological evolution: electromigration-induced formation of faceted slits, and stress-induced formation of fine-scale crack-like features on the void surface. In [32] current-induced morphological evolutions of void surfaces were studied theoretically and numerically, accounting for surface diffusional anisotropy. The non-linear analysis predicted a surface morphological transition, and the onset of oscillatory dynamics at a critical strength of the applied electric field. Migration of voids along the film at constant speed, with steady and time-periodic surface morphologies was also studied, for electric fields weaker and stronger than critical. In a recent study [24] they presented a multiscale modeling approach for the analysis of morphological evolution and electromigration failure in ductile metallic thin films of integrated circuits. In [27] they presented the effects of anisotropy of void surface diffusivity on the stability of the interconnects. They predicted formation of stable faceted voids and wedge-shaped voids, and studied failure due to propagation of slit-like features from void surfaces. In [26] they considered morphological instabilities caused by simultaneous action of applied mechanical stress and electric field on transgranular dynamics of voids, and studied propagation of slits. They predicted by numerical simulations that a failure might occur by the coupling of two modes of surface morphological instability. These extensive and broad analyzes may be instrumental for the design of integrated circuits, by allowing to predict the reliability and the lifetime of an interconnect.

Schimschak and Krug [29] proposed a continuum description of the surface evolution that takes into account electromigration and capillarity-driven surface diffusion. For numerical simulations they applied a one-dimensional model of interface dynamics, which can be parameterized by a height function. The one-dimensional geometry is convenient and relevant to the modeling of shape changes at the edge of an effectively two-dimensional conductor line, but becomes inappropriate if the dynamics create overhangs. In [28] they studied numerically the motion and shape evolution of an infinitely extended, isotropic, and homogeneous two-dimensional current-carrying conductor, considering a series of morphological transitions and conditions of instability for initially circular voids. The electromigration-induced shape evolution of cylindrical voids was numerically examined in [15], accounting for mass transport, current crowding, and crystal anisotropy in the surface mobility. The authors considered finite strips with periodic boundary conditions in the current direction, and voids in infinite or semi-infinite strips.

Mahadevan et al. [16] studied an edge instability in single-crystal metal lines, applying a numerical phase field technique. The authors defined the critical value of the applied current when the edge perturbation

grows to become a slit-shaped void that spans the wire and leads to electrical failure, reducing the circuit lifetime to an unacceptable level. The phase field model [17] provides an attractive alternative in which the interface is not explicitly tracked. In the phase field approach, the idea of a sharp interface between metal and void is abandoned. Instead, the thin film and the space around it are described by a continuous and rapidly varying scalar function, called an order parameter. It accepts specific distinct uniform values well within the metal and well inside the void.

There is an apparent analogy between the level set method [4,5,42–45] and the phase field method. Averbuch et al. [7] and Nathan et al. [60] applied the level set approach to study the drift electromigration in metal lines of microelectronic interconnects. In the level set, the level function is usually a signed distance from the given point to the interface line. The distance is considered negative in the void and positive in the conducting medium. Applying the hyperbolic tangent to the scaled distance function, one gets a parameter of phase field. Indeed, this leads to unity well inside a metal and minus unity well in a void. The scaling parameter adjusts the rapidly or slowly varying function.

Mahadevan and Bradley [30] used a phase field method to simulate the time evolution of a perturbation to the edge of a current-carrying, single-crystal metal line, accounting for electromigration, surface diffusion and current crowding. The authors provided a fabrication criterion that ensured the wire will not fail through formation of voids. In this case the edge perturbations are small enough so that the operating current does not exceed the threshold, and the instability through the formation of slit-shaped voids does not occur. An alternative approach to increase the lifetime of the interconnect is to orient appropriately the crystal with respect to the applied field.

The phase field principle, with an order parameter characterizing the damaged state of the interconnect, was further used by Bhate et al. [18,31] for simulating electromigration and stress-induced void evolution. The evolution of the order parameter was governed by a fourth-order parabolic PDE, related to the Cahn–Hilliard equation [19]. Bhate et al. solved the PDE by an implicit finite element scheme together with the accompanying mechanical (elastic) and electrical problems.

Fridline and Bower [20] studied the effect of the anisotropy of the surface diffusivity on the formation and growth of slit-like voids, considering an interconnect as a two-dimensional electrically conducting strip that contains an initial semi-circular void. They applied a finite element model to predict the evolution of the void after an electric field was applied to the strip. Their later work [25] accounts for several kinetic processes involved in interconnect failures, including surface diffusion, interface and grain boundary diffusion, and sliding on grain boundaries and at the interface between line and elastic passivation.

Gray et al. [35] applied an approximate Green's function to solve the Laplace equation for the electric potential by the boundary element method, in order to model the void dynamics under electromigration conditions in metallic thin-film interconnects. The approximate Green's function was constructed by reflecting the source point through a plane. The method retains the primary attribute of an exact Green's function: elimination of surfaces from the calculation. Another application of the method is the simulation of the industrial electroforming process. A boundary element approach was applied by Averbuch et al. [8] for numerical studies of the electromigration in metal films of microelectronic interconnects with a polycrystalline structure, with the external electric field parallel to the grain boundary.

Suo [37] considered aluminum interconnects in the presence of insulators and shunts, subjected to temperature change and a direct electric current. He studied the evolution of interconnects into a stable state with a segment of aluminum depleted near the cathode, a linear distribution of pressure in the rest of the line, and no further mass diffusion, and estimated the time scale for the interconnect to evolve to the stable state. In [36] he described the mechanisms for diffusive processes in solid structures of small feature sizes, between a few to hundreds of nanometers. Considering microelectronic and photonic devices, he applied the concept of free energy. The change of free energy defines a thermodynamic force which, in its turn drives the configurational change of the structure. The author gave a physical description of forces of

diverse origins that occur in thin films of interconnect lines, including elasticity, electrostatics, capillarity, electric current, and others. Yu and Suo [38] derived a finite element formulation to model the dynamics of a single pore on a moving grain boundary, assuming that surface diffusion is the dominant process for a small pore to adjust its shape and position.

Sun et al. [39] considered the evolution of grains in a polycrystalline fiber, and applied a variational approach to microstructure development, which incorporates thermodynamic forces and mass transport mechanisms. The free energy included interfacial, elastic, electrostatic and chemical components. The rate process included diffusion, creep, grain-boundary motion, and surface or interface reactions. In a later work, Sun et al. [40] modeled the dynamics of a two-grain thin film on a substrate. They developed a finite element formulation that accounted for surface tension anisotropy, bulk phase free energy density, and finite junction mobility. The authors formulated the laws for the motion and equilibrium of triple junctions, and considered the motion of grain–void interfaces and grain boundaries. The large shape changes of a solid due to matter diffusion on its surface were studied by Sun and Suo [41]. In addition to surface diffusion, evaporation and condensation were accounted for, and the finite element approach was applied to analyze the thermal grooving on a polycrystalline surface.

Haen et al. [51] performed electromigration experiments in a scanning electron microscope (SEM), and took images over the length of a metal line subjected to high current and temperature stress. Comparison of the electrical resistance curves with the SEM and AFM (atomic force microscope) micrographs makes it possible to correlate the observed variations of resistance with changes in microstructure of the stripe, although extensive voids can exist in the line even without noticing this from the resistance change curve. They observed phenomena like growth of voids along grain boundaries, the merging of several voids into one larger void, and the opposite process where a large void splits up into several smaller ones. It was discovered that some voids that were growing fast in the initial stage of the electromigration tended to stabilize.

Ben Amar et al. [52] investigated analytically and numerically the void electromigration process in the strip geometry. The authors adapted conformal mapping techniques to predict the shapes of steady voids traveling in the middle of the strip. They found that only time-dependent solutions can travel along at the boundary, and used asymptotic methods to model this motion.

The asymmetrical evolution of voids in an infinite two-dimensional space was simulated by Gao et al. [53], focusing on an elliptical void and the shape asymmetry with respect to the direction of the remote electric field. They examined numerically the translation of the void, rotating its orientation and changing its initial shape, and studied the conditions under which the void can evolve eventually to a steady shape.

Rice and Chuang [54] discussed the approaches for calculation of chemical potentials and energy-released rates for the growth of creep cavities along the grain boundaries, accounting for thermodynamic restrictions on the angle formed by the void surfaces at their apex. The authors noted that the actual requirement of thermodynamics for quasi-static isothermal crack growth should be phrased as the inequality assuring non-negative entropy production. Considering the representative cases, they revealed that the strain-energy contributions to chemical potentials on grain boundaries and free surfaces are negligible. The authors showed that the major sink of energy in cavity growth is from the work of normal stresses on the effective opening of the grain boundary due to the addition of matter by diffusion.

Oren and Ogurtani [55] developed a mathematical model of the mass flow and accumulation on void surfaces under the action of applied electrostatic force fields and capillary effects that follows from the conservation laws, and from fundamental postulates of linear irreversible thermodynamics, accounting for the effects of applied electric field and thermal stress. The authors considered both the drift diffusion of chemical species on the void surface, and the direct transfer of chemical species between bulk phase and the void region through the interface layer. It follows from the relationship for the integrated entropy production derived by Ogurtani that any configuration and/or kinematic singularities along the curved interface (discontinuity in slope, curvature, flux) result in extra internal entropy production as a point

entropy source. In particular, this leads to a conjugate flux at the triple point, proportional to the jump of curvatures between the two branches of the interface. This, in turn, results in a transfer of matter from the branch with the small curvature to that with the large one, or from the branch with the negative curvature to that with the positive one. This transfer will lead to a decrease of initial differences in curvatures, and there will be always transfer of matter from hills to valleys. This process will take place even if there is no local change in curvature vs. interface arclength at each branch of the interface considered separately in the proximity of the triple point. That is to say, if the two branches are initially circular arcs of different radii (or, maybe, radii of different signs, concave and convex), the local derivatives of curvature will vanish on both sides, but there will still be a motion at the triple point associated with the conjugate flux.

Numerical simulations in [55] were run with and without the surface diffusion anisotropy, with the initial void shape critical-asymmetric with respect to the direction of electron flow. These numerical experiments show that the twofold asymmetry in the anisotropic diffusion coefficient becomes a main factor in the development of a straight advancing slit, which accelerates the early open circuit failure due to a sharp slit hitting the upper edge of the interconnect. This phenomenon was also observed by scanning electron microscopy experiments [50]. The fourfold asymmetry and, to a lesser extent, the sixfold asymmetry lead to the development of the straight advanced front (faceting) that results in the open circuit failure due to a wedge-shaped void hitting the upper edge of the interconnect. The effective time to failure increases as the degree of the surface anisotropy increases. Considering the initial void shape uncritically asymmetric to the direction of the electron flow, they observed that the void shape was first converted into a critical form, and then a fragmentation into a wedge-shaped daughter cell took place. These observations can be utilized in the design rules for interconnect thin films with bamboo structure. In their later study [56], Oren and Ogurtani developed a model for the void configurational evolution during the intergranular motion, considering the generalized forces, the conjugate fluxes, and the energy dissipation at a triple junction in multi-component systems. The authors note that of the normally used three boundary conditions at the triple point – the continuity of the chemical potential, the equilibrium capillarity configuration for geometry, and the conservation of mass – the first two are mutually incompatible. Considering the internal entropy production associated with the virtual displacements of the junction, and applying the laws of linear thermodynamics only, they deduced (longitudinal and transverse) the displacement velocities of the triple junction. Numerical simulations of the intergranular void dynamics showed that the existence of grain boundaries aligned normal to the direction of the electron wind resulted in a great improvement in the circuit failure time, compared to the single crystal interconnect made by the same material having similar crystalline planes and orientations.

Huang et al. [57] developed a finite element model to simulate the diffusive growth of the grain boundary voids under external tension, considering both the surface diffusion and grain boundary diffusion coupled by boundary conditions at the triple point of the void surface and the grain boundary. The numerical simulations showed that the rate of void growth is related to the ratio of the two diffusivities (diffusivity of the grain–void interface, and that of the grain boundary). The prevailing of grain boundary diffusion over surface diffusion, high external tensile stress, and small spacing between the voids result in an elongation of the void in the direction of the grain boundary, with the void attaining a long crack-like configuration.

Liu et al. [58] considered a steady-state crack growth along a grain boundary for different combinations of signs of crack tip angles at the triple point, in an interconnect subjected to a high current density, and studied the crack propagation transverse to the remote electric field. The crack width and growth rate were found to be proportional to $E^{-1/2}$ and $E^{3/2}$, respectively, where E is the applied external electric field. Therefore, the life-time of the interconnect is expected to be proportional to $E^{-3/2}$.

The kinetics of void growth in unpassivated, electroplated copper lines were studied by Liniger et al. [59]. The experimental investigation with the scanning electron microscope aimed to study the effect of sample temperature and linewidth on the rate of void growth. Voids were observed to grow by consuming grains in

a stepwise fashion, either by thinning out from the top down, or through a simple edge displacement mechanism. In all cases, surface diffusion was the primary diffusion path for void growth. In the case of polycrystalline lines, grain boundaries provided a secondary path for copper diffusion. Hillock formation was observed close to the anode end of the test lines. Over time, hillock formation spread over the entire length of the line with the exception being the area just around the cathode end of the test structure. Voiding was observed to initiate at the cathode end of the line, and to grow along an apparent grain boundary. After some time, the void grew across the entire width of the line, leaving behind a small island of copper. Significant variation of thickness in metal lines was observed by Augur et al. [61]. Aluminum layers showed damage by local thinning. The mechanism underlying this failure is caused by grain boundary grooving and interface diffusion, and leads to substantial metal transport.

An electromigration problem with a specific geometry is solved in our study by a different numerical approach. We applied a parametric presentation of the curved interface between an external void and the bulk material in the Cartesian space. In addition, the application of the cubic spline technique to rearrange the generating points of the interface line in a uniform manner allows to apply standard methods of finite difference of any order. With this approach, one may omit continuous or systematic application of the remeshing and elimination procedure on irregularly disposed nodes.

3. Physical formulation

3.1. Governing PDE

We consider a conducting metal bamboo line, typical of modern sub-micron interconnects, made of a thin metal strip attached to a substrate, as shown in Fig. 1. The strip is attached to electrodes at its ends AA_1D_1D and BB_1E_1E. Vector $\boldsymbol{E}$ indicates the direction of the external electric field. The resistance of the substrate is assumed infinite. Irregularities are assumed to occur on the top surface AA_1B_1B only. Fig. 1(a) shows a strip sector with a single grain, while Fig. 1(b) shows a two-grain sector. The grain boundary TT_1C_1C is assumed planar. This planar surface is assumed parallel to axis z, and may be normal or tilted with respect to the horizontal surface of the substrate xz. TT_1 is a top "triple line", and CC_1 is a bottom triple line. Line CC_1 is assumed to be immobile or "pinned" at the substrate. Pinning of a grain boundary is normally attributed to solute or second phase particles, and represents a specific case. In future work, this condition will be relaxed. L_y is the line thickness, and L_z is the line width.

We assume that the surface curvature and the voltage gradient in the z-direction may be neglected, and consider the two-dimensional scheme of the bamboo line shown in Fig. 2. The top side of the metal strip is considered a curvilinear grain–void interface. Assume that this curved void boundary is set parametrically in the Cartesian space

$$x = x(r), \quad y = y(r), \tag{2}$$

where r is a parameter independent of time. The evolution equations are [5]

$$\dot{x} = F\frac{y'}{g}, \quad \dot{y} = -F\frac{x'}{g}, \tag{3}$$

where dot denotes time derivative, and prime denotes spatial derivative (with respect to parameter r). The present arclength cannot be used as a parameter since it is time-dependent, but the arclength of the initial configuration or other reference configuration can be used. g is the metric function, which is defined as

$$g = \frac{\mathrm{d}s}{\mathrm{d}r} = \sqrt{x'^2 + y'^2} \tag{4}$$

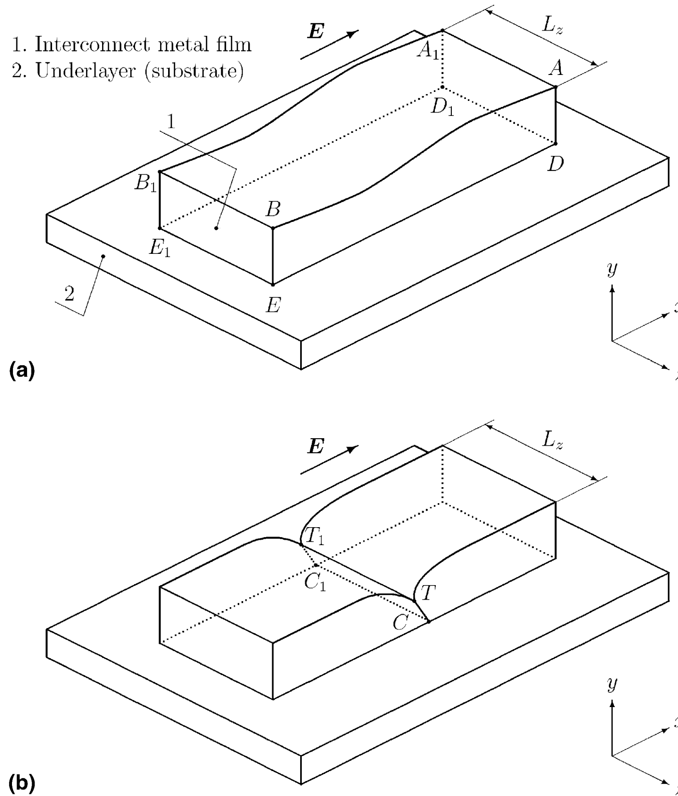

Fig. 1. Three-dimensional scheme of bamboo line: (a) single-grain sector of interconnect; (b) two-grain sector of interconnect.

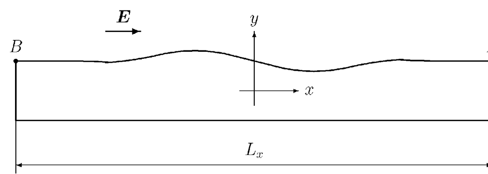

Fig. 2. Single grain in a bamboo line.

and F is the normal velocity of the front defined by Eq. (1). It includes the second derivative of the curvature and that of the voltage with respect to the present (time-dependent) arclength. The voltage distribution will be discussed in Section 5.

3.2. Boundary conditions for single grain

For a single grain–void interface, the boundary conditions are set at the end points of the interconnect line A and B (Fig. 2), where the electrodes are attached. We assume that there is no flux at the electrode points

$$K_s^A + \alpha U_s^A = 0, \quad K_s^B + \alpha U_s^B = 0. \tag{5}$$

Thus, the derivative of curvature at the electrode points does not vanish, and is proportional to the electric field.

We assume that the slopes of the grain–void interface are zero at the end points

$$\frac{dx}{ds} = -1, \quad \frac{dy}{ds} = 0. \tag{6}$$

We pass the contour of the interconnect in the counter-clockwise direction, so that its top side is passed from the right to the left. The arclength increases when moving from point A to point B.

3.3. Continuity conditions for an intergranular groove

Voids often occur on the grain boundaries, and thus, studying their surface diffusion and electromigration requires some intergranular analysis [1]. A two-grain portion of a bamboo line is shown in Fig. 3. β is the tilt angle of the intergranular boundary with respect to a plain interface line that is assumed to have no irregularities (and also with respect to the direction of the external electric field). The intergranular groove evolves under surface diffusion and electric field forces. We assume for simplicity that the grain boundary TC contributes no additional electric resistance, that the specific resistances of both grains are the same, and that mechanical equilibrium holds at the triple point T. In general, the specific surface energy (per unit length of the grain–void boundary) is different for grains 1 and 2 (anisotropic case). In this study, however, we consider only the particular isotropic case of equal surface tensions γ^S. Therefore, at the triple point, the angles θ between the tangent line to the intergranular boundary and the tangent lines to the void interface contour are the same for both grains

$$\gamma_1^S = \gamma_2^S \rightarrow \theta_1 = \theta_2 \stackrel{\text{def}}{=} \theta. \tag{7}$$

In addition to the boundary conditions at the electrode points, two continuity conditions are applied for the triple point T.

3.3.1. Conservation of material

The diffusion flux J_0 along the grain boundary is induced by the voltage gradient U_g along the boundary and the derivative of the stress S_g

$$J_0 = \tilde{\alpha} U_g - \tilde{\gamma} S_g, \tag{8}$$

where $\tilde{\alpha}$ and $\tilde{\gamma}$ are constant coefficients depending on the elastic and electro-chemical properties of the material, and $\tilde{\alpha}$ differs from α in Eq. (1), although they have the same units. The voltage gradient along the grain boundary may be approximated by the projection of the external field

$$U_g \approx E_{ext} \cos\beta = \frac{U^B - U^A}{L_x} \cos\beta, \tag{9}$$

where U^B and U^A are potentials applied to the left and right ends of the metal line, respectively, and L_x is the length of the line. Due to the conservation of material, the jump in the flux ΔJ at the triple point T between the right and the left branches of the grain–void interface is equal to the flux J_0 along the grain boundary

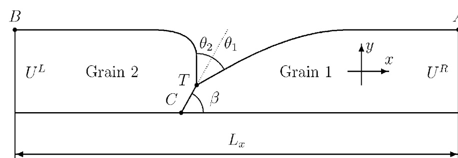

Fig. 3. Two-grain bamboo line.

$$\Delta J \stackrel{\text{def}}{=} J^{\mathrm{R}} - J^{\mathrm{L}} = J_0. \tag{10}$$

The flux at the grain–void interface is defined as

$$J = K_s + \alpha U_s, \tag{11}$$

where α is the ratio between the electric field forces and the surface diffusion. Note that after normalization of the time in Eq. (1) $\tau = Bt$, the new α becomes α/B and B becomes unity. The external field is considered positive when directed from the left to the right, i.e., in positive x. Eq. (10) becomes

$$\left(K_s^{\mathrm{R}} + \alpha U_s^{\mathrm{R}}\right) - \left(K_s^{\mathrm{L}} + \alpha U_s^{\mathrm{L}}\right) = \tilde{\alpha}\frac{U^B - U^A}{L_x}\cos\beta + \tilde{\gamma}S_{\mathrm{g}}. \tag{12}$$

We assume here that there is no flux along the grain boundary TC at point C (Fig. 3), where this boundary meets the substrate. Since there is no accumulation or depletion of the material along the grain boundary, the flux along TC is constant, i.e., it vanishes at every point. That is to say, the effect of the voltage gradient in Eq. (8) is totally compensated by the influence of the stress: $J_0 = 0$. In particular, the surface flux along the grain boundary vanishes at the triple point T. Thus, it follows that the flux at the triple point is continuous

$$J^{\mathrm{R}} = J^{\mathrm{L}}, \tag{13}$$

and the right-hand side of Eq. (12) vanishes. This is, of course, an approximate simplified approach: in a real system, there is some flux along the grain boundary. The conservation of material holds in the model: since the fluxes at the electrode points vanish and the flux at the triple point of the grain–void interface is assumed continuous, the area of the interconnect in plane xy remains constant during the evolution, i.e., $\mathrm{d}A/\mathrm{d}t = 0$. Our model is 2D, but actually this means that the volume is constant. Note that although the interface flux is continuous at the triple point, it is not zero, and there is an exchange of metal between two grains. The total mass of two grains is constant, but the mass of each grain is not.

3.3.2. Existence of triple point

We assume that the intergranular boundary is initially a straight line (a planar surface in three-dimensional formulation), and remains a straight line under the evolution. At the triple point, projections of the normal velocities in the direction of the intergranular boundary should be the same, otherwise the triple point does not exist. Since we consider the isotropic case when the triple angles θ are the same for both branches of the interface, there is a continuity of the front velocity

$$F^{\mathrm{L}} = F^{\mathrm{R}} \quad \text{or} \quad K_{ss}^{\mathrm{L}} + \alpha U_{ss}^{\mathrm{L}} = K_{ss}^{\mathrm{R}} + \alpha U_{ss}^{\mathrm{R}}. \tag{14}$$

4. Finite difference formulation of diffusion component

To solve the governing PDEs (Eqs. (1) and (3)), we apply a finite difference discretization on a regular grid in space, and a Runge–Kutta integration scheme in time. These equations are solved simultaneously with a static Laplace equation describing the voltage distribution. The solution of the Laplace equation is updated in each time step.

4.1. Finite differences at internal points

Recall that the grain–void interface line $[x(r), y(r)]$ is described parametrically, where r is the time-independent parameter. The second derivative of curvature with respect to the arclength constitutes a diffusion component of the front velocity, and is defined as

$$K_{ss} = \frac{\mathrm{d}K_s}{\mathrm{d}s} = \frac{\mathrm{d}r}{\mathrm{d}s}\frac{\mathrm{d}K_s}{\mathrm{d}r} = \frac{1}{g}\frac{\mathrm{d}}{\mathrm{d}r}\frac{K'}{g} = \frac{K''g - K'g'}{g^3}. \tag{15}$$

It follows from Eq. (4)

$$g' = \frac{x'x'' + y'y''}{g}. \tag{16}$$

Thus, the metric function g and its derivative g' are not new functions to be considered, but only new notations. The curvature K is defined as

$$K = \frac{y''x' - x''y'}{g^3}. \tag{17}$$

Thus, the governing set (3) includes two coupled PDEs of fourth order in space and first order in time.

Assume that the interface line is set initially by a sequence of generating points $(x_0, y_0), (x_1, y_1), \ldots, (x_N, y_N)$, not necessarily equally spaced. At first, we use as a parameter the normalized number of the current point $r = i/N$. Applying the cubic spline technique, we rearrange the generating points of the interface line in a uniform manner. Now the points are equally spaced along the arclength, and we use the arclength of the initial configuration as a parameter. Since the slopes are specified at the end points, the derivative boundary conditions are applied at the ends of the spline

$$x_i = x(s_i), \quad y_i = y(s_i), \quad s_i - s_{i-1} = \Delta s = \text{const.} \tag{18}$$

Note that the arclength of the present configuration depends on time, while that of the initial configuration obviously does not. Since the arclength is used as a parameter, at $t = 0$ the metric is identically unity, and its spatial (arclength) derivative vanishes everywhere

$$g(s) \equiv 1, \quad g'(s) = 0 \tag{19}$$

and we use Eq. (19) when we start the first step in time.

For the arclength used as a parameter, the second derivative of curvature becomes

$$K_{ss} = \left(y''x' - x''y'\right)'' = y^{\mathrm{IV}}x' - x^{\mathrm{IV}}y' + y'''x'' - x'''y''. \tag{20}$$

However, instead of direct calculation of the third and fourth derivatives, it is advantageous and suitable to establish the first and second derivatives of the Cartesian components in order to approximate the curvature, and then to calculate the second derivative of the curvature. For all grid points, except the triple points and the nodes immediately adjacent to the triple point, central differences can be applied:

$$\begin{aligned}
x'(s) &= \frac{x(s+\Delta s) - x(s-\Delta s)}{2\Delta s}, \\
y'(s) &= \frac{y(s+\Delta s) - y(s-\Delta s)}{2\Delta s}, \\
x''(s) &= \frac{x(s+\Delta s) - 2x(s) + x(s-\Delta s)}{\Delta s^2}, \\
y''(s) &= \frac{y(s+\Delta s) - 2y(s) + y(s-\Delta s)}{\Delta s^2}, \\
K(s) &= y''(s)x'(s) - x''(s)y'(s), \\
K''(s) &= \frac{K(s+\Delta s) - 2K(s) + K(s-\Delta s)}{\Delta s^2}.
\end{aligned} \tag{21}$$

The scheme is of second-order accuracy, and the local truncation error for the second derivative of curvature is equal to

$$E = \left(y'''x^{\mathrm{IV}} - x'''y^{\mathrm{IV}} + 3y''x^{\mathrm{V}} - 3x''y^{\mathrm{V}} + 2y'x^{\mathrm{VI}} - 2x'y^{\mathrm{VI}}\right)\frac{\Delta s^2}{12}. \tag{22}$$

4.2. End points and neighbor-to-end nodes

For end points and adjacent nodes, the boundary conditions are used. To find the second derivative of curvature, we apply a one-sided (forward or backward) difference, using the values of the curvature and the given value of its derivative at the triple point. Assume that a second-order accuracy is required for the second derivative of curvature at the end points too (as well as for the internal points). Assume that there are $N^{\mathrm{R}} + 1$ nodes on the right branch of the interface line, numbered from 0 to N^{R}, and $N^{\mathrm{L}} + 1$ nodes on the left branch with independent enumeration from 0 to N^{L}, as shown in Fig. 4. Note that N^{R} and N^{L} are the corresponding amounts of grid intervals. For the right branch of the interface line, node 0 is the end point, and N^{R} is the triple point T. For the left branch, node 0 is the triple point T, and node N^{L} is the end point. Node 1 of the right branch and node $N^{\mathrm{L}} - 1$ of the left branch are neighbors-to-ends.

For a uniform symmetric grid, the finite difference approximation of the second derivative with the second-order accuracy includes three node values. However, we cannot apply the symmetric formula for end nodes, and since the grid ceases to be symmetric, one more node value is required. This will be the node value of the first derivative of curvature at the triple point. We introduce the following notations: A and B for the end points, and a and b for the corresponding adjacent nodes, as shown in Fig. 4. For end point A let us seek the difference approximation for the second derivative of the curvature in the following form:

$$K_{ss}^{A} = \frac{C\Delta s K_s^A + C_0K_0 + C_1K_1 + C_2K_2}{\Delta s^2}, \tag{23}$$

where C, C_0, C_1 and C_2 are coefficients to be established. The error should be of order Δs^2. Expanding K_1 and K_2 into the Taylor series in the proximity of the triple point A till $O(\Delta s^4)$ and neglecting the high order terms, we obtain:

$$\begin{aligned} K_1 &= K(s+\Delta s) = K_0 + K_0'\Delta s + \frac{K_0''\Delta s^2}{2} + \frac{K_0'''\Delta s^3}{6} + \frac{K_0^{(4)}\Delta s^4}{24}, \\ K_2 &= K(s+2\Delta s) = K_0 + 2K_0'\Delta s + 2K_0''\Delta s^2 + \frac{4K_0'''\Delta s^3}{3} + \frac{2K_0^{(4)}\Delta s^4}{3}, \\ s &= 0. \end{aligned} \tag{24}$$

Introducing Eq. (24) into (23) and balancing the terms, we get the following solution:

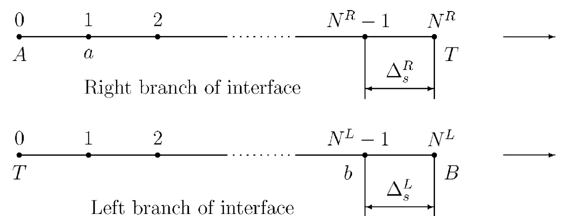

Fig. 4. Grid for an interface line.

$$\begin{cases} C_0 + C_1 + C_2 = 0, \\ C + C_1 + 2C_2 = 0, \\ C_1 + 4C_2 = 2, \\ C_1 + 8C_2 = 0, \end{cases} \qquad \begin{cases} C = -3, \\ C_0 = -7/2, \\ C_1 = 4, \\ C_2 = -1/2. \end{cases} \tag{25}$$

Thus, the difference approximation and the leading error term become

$$K_{ss}^A = \frac{-6\Delta s K_s^A - 7K_0 + 8K_1 - K_2}{2\Delta s^2} - \frac{K_0^{(4)}\Delta s^2}{6}. \tag{26}$$

The higher order terms are neglected. For K_{ss}^a, a central difference can be used

$$K_{ss}^a = \frac{K_0 - 2K_1 + K_2}{\Delta s^2} - \frac{K_1^{(4)}\Delta s^2}{12}. \tag{27}$$

Should we desire to get a truncation error $O(\Delta s^2)$, then the values of K_0, K_1 and K_2 should be estimated with the accuracy $O(\Delta s^2)$. This means that the first and the second derivatives of x and y at these points should be of fourth-order accuracy.

At end points A and B and at triple point T, the first derivatives x' and y' are set exactly. A similar technique of undetermined coefficients, which was used for the second derivative of curvature, yields the first derivatives at two other points. For point A and neighbor point a:

$$\begin{aligned} x_1' &= \frac{-6\Delta s x_A' - 17x_0 + 9x_1 + 9x_2 - x_3}{18\Delta s} - \frac{x_1^{(5)}\Delta s^4}{60}, \\ x_2' &= \frac{3\Delta s x_A' + 7x_0 - 18x_1 + 9x_2 + 2x_3}{9\Delta s} + \frac{x_2^{(5)}\Delta s^4}{30}. \end{aligned} \tag{28}$$

The second derivatives are:

$$\begin{aligned} x_0'' &= \frac{-300\Delta s x_A' - 415x_0 + 576x_1 - 216x_2 + 64x_3 - 9x_4}{72\Delta s^2} - \frac{x_0^{(6)}\Delta s^4}{15}, \\ x_1'' &= \frac{60\Delta s x_A' + 257x_0 - 480x_1 + 252x_2 - 32x_3 + 3x_4}{144\Delta s^2} + \frac{x_1^{(6)}\Delta s^4}{360}, \\ x_2'' &= \frac{-x_0 + 16x_1 - 30x_2 + 16x_3 - x_4}{12\Delta s^2} - \frac{x_2^{(6)}\Delta s^4}{90}. \end{aligned} \tag{29}$$

Similar equations are used for derivatives of y. We calculate the curvature using the first and second derivatives of x and y, according to Eq. (17). For the other end point B and neighbor point b, the difference approximations are derived in a similar manner.

4.3. Derivatives of curvature at a triple point

At the triple point, the slopes are set exactly, but the arclength derivative of curvature is not specified. Thus, we cannot apply Eq. (26) directly to establish K_{ss} at the right and left branches of the triple point, but have to use it in combination with the continuity conditions, Eqs. (12) and (14). Applying Eq. (26) for the right and left branches at their junction T, we obtain:

$$\begin{aligned} K_{ss}^{\mathrm{R}} &= \frac{6\Delta_s^{\mathrm{R}} K_s^{\mathrm{R}} - 7K_{N^{\mathrm{R}}} + 8K_{N^{\mathrm{R}}-1} - K_{N^{\mathrm{R}}-2}}{2\Delta_s^{\mathrm{R}^2}}, \\ K_{ss}^{\mathrm{L}} &= \frac{-6\Delta_s^{\mathrm{L}} K_s^{\mathrm{L}} - 7K_0 + 8K_1 - K_2}{2\Delta_s^{\mathrm{L}^2}}, \end{aligned} \tag{30}$$

where Δ_s^R and Δ_s^L are grid intervals for the right and left branches, respectively, as shown in Fig. 4. These grid intervals may be different for two branches.

We introduce notation Z_s^R and Z_s^L, related to the right and left branches, respectively. These values can be calculated directly and have units of derivative of curvature with respect to arclength

$$Z_s^R = \frac{-7K_{N^R} + 8K_{N^R-1} - K_{N^R-2}}{2\Delta_s^R}, \quad Z_s^L = \frac{-7K_0 + 8K_1 - K_2}{2\Delta_s^L}. \tag{31}$$

Eq. (30) leads to

$$K_{ss}^R \Delta_s^R - 3K_s^R = Z_s^R, \quad K_{ss}^L \Delta_s^L + 3K_s^L = Z_s^L. \tag{32}$$

Auxiliary Eq. (32), in combination with the continuity conditions (Eqs. (12) and (14)), leads to a linear set that makes it possible to establish the first and the second derivatives of curvature at both branches of the triple point: K_s^R, K_s^L, K_{ss}^R and K_{ss}^L. We introduce the following notations:

$$\begin{cases} A_s = \alpha(U_s^R - U_s^L) + J_0, \\ A_{ss} = \alpha(U_{ss}^R - U_{ss}^L), \end{cases} \tag{33}$$

$$\begin{aligned} &\Delta s = \Delta_s^R + \Delta_s^L, \quad Z_s = Z_s^R + Z_s^L, \\ &D = \frac{\Delta_s^R Z_s^L - \Delta_s^L Z_s^R}{3\Delta s}, \quad Q = \frac{A_{ss}\Delta_s^R \Delta_s^L}{3\Delta s}. \end{aligned} \tag{34}$$

The flux J_0 along the grain boundary is assumed vanishing. We get the solution of the equation set for an arbitrary flux, and then we set the flux J_0 to zero. With the above notations, the solution is

$$\begin{cases} K_s^R = -\frac{A_s\Delta_s^R}{\Delta s} + D - Q, \quad K_s^L = +\frac{A_s\Delta_s^L}{\Delta s} + D - Q, \\ K_{ss}^R = \frac{-3A_s - A_{ss}\Delta_s^L + Z_s}{\Delta s}, \qquad K_{ss}^L = \frac{-3A_s + A_{ss}\Delta_s^R + Z_s}{\Delta s}. \end{cases} \tag{35}$$

Note that the voltage distribution problem is already solved by that time, so that the derivatives of voltage U_s^R, U_s^L, U_{ss}^R and U_{ss}^L are all known values.

Fluxes on the right and left interface branches at the triple point are

$$J^R = \frac{B_u}{\Delta s} + D - Q + J_0\frac{\Delta_s^R}{\Delta s}, \quad J^L = \frac{B_u}{\Delta s} + D - Q - J_0\frac{\Delta_s^L}{\Delta s}, \tag{36}$$

where

$$B_u = \alpha(U_s^R \Delta_s^L + U_s^L \Delta_s^R). \tag{37}$$

The normal velocity F_T at the triple point, which, for the isotropic case, is the same for both branches, becomes

$$F_T = K_{ss}^R + \alpha U_{ss}^R = K_{ss}^L + \alpha U_{ss}^L = \frac{-3A_s + A_u + Z_s}{\Delta s}, \tag{38}$$

where

$$A_u = \alpha(U_{ss}^R \Delta_s^R + U_{ss}^L \Delta_s^L). \tag{39}$$

In particular, when no external voltage is applied to the interconnect (evolution under surface diffusion only), both K_s and K_{ss} are continuous at the triple point. If, in addition, the problem is symmetric ($\beta = \pi/2$) as in the classical Mullins formulation [46], the value D vanishes, and this yields $K_s^R = K_s^L = 0$.

4.4. Tangential motion at the proximity of a triple point

The scheme of tangential motion is presented in Fig. 5. T is the position of the triple point before marching in time, which takes into consideration only the normal motion of the curve. Therefore, after one-step marching is done, the new locations of the triple point on the right and left branches, T^{R} and T^{L} may not belong to the intergranular boundary. Depending on the sign of the front velocity, they will be either ahead or behind the intergranular boundary. In Fig. 5, they are shown ahead of the boundary, i.e., the new contour lines AT^{R} and BT^{L} do not intersect the intergranular line CT. Points T^{R} and T^{L} are not true triple points, since they do not belong to the interface between two grains. In Fig. 5, the solid line is the grain–void boundary before marching, the dot line – after marching. Vectors TT^{R} and TT^{L} are normal shifts of the triple point, and they are fairly small with respect to the arclength grid interval since $\Delta\tau \sim \Delta s^4$, due to stability requirements of the explicit difference scheme.

For the new grain–void interface line, one may apply the spline extrapolation technique with derivative boundary conditions at the end of the spline. Extrapolation should be used when the new triple points T^{R} and T^{L} are ahead of the intergranular boundary, and interpolation when these points are behind that boundary. Since the normal shifts are small with respect to the spline grid, the interpolation or extrapolation points are very close to the end nodes of the spline, and the accuracy of extrapolation is good. Assuming that the intergranular boundary passes through the origin of the Cartesian frame, the spline equation becomes

$$x(s)\sin\beta = y(s)\cos\beta \tag{40}$$

and it has to be solved for the unknown arclength s for either the left or the right branch. β is the tilt angle of the intergranular boundary defined in Fig. 3. Due to continuity conditions, both branches lead to the same location of the triple point T'.

Since both normal and tangential shifts are very small, one may apply a linear interpolation instead of a cubic spline, without any essential loss of accuracy. According to the scheme in Fig. 5, the normal shifts are

$$|TT^{\mathrm{R}}| = |TT^{\mathrm{L}}| = F_{\mathrm{T}}\Delta t, \tag{41}$$

where F_{T} is the normal front velocity at the triple point, taken as the average value for two swaps of Runge–Kutta 2. The shift along the intergranular boundary is

$$|TT'| = \frac{F_{\mathrm{T}}\Delta t}{\sin\theta}. \tag{42}$$

The tangential shifts are

$$|T^{\mathrm{R}}T'| = |T^{\mathrm{L}}T'| = F_{\mathrm{T}}\Delta t\cot\theta. \tag{43}$$

Now the triple points of a new grain–void interface are located at the intergranular boundary, and we rearrange the splines for these new ends. After re-arrangement, the nodes of the spline are equally spaced along the arclength of each branch.

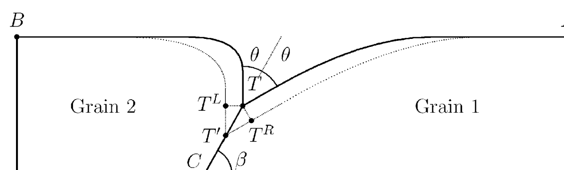

Fig. 5. Tangential motion of an interface line.

4.5. Runge–Kutta integration scheme

The explicit Runge–Kutta scheme is applied for marching in time. Since the governing PDE is of the fourth order in space, the time step should be limited to provide a stable integration

$$\Delta t = k_z \frac{\Delta s^4}{B}, \tag{44}$$

where k_z is a dimensionless coefficient. Numerous simulations show that for the governing PDEs (1), (3) it should not exceed 1/35. Since the time step defined by stability requirements is very small, there is no need to apply Runge–Kutta schemes of high orders. We use order 2. After discretization in space, the PDE converts into a set of ODEs:

$$\begin{cases} \dot{x}_i = [K_i''(\boldsymbol{x},\boldsymbol{y}) + \alpha U_i''(\boldsymbol{x},\boldsymbol{y})]y_i' \overset{\text{def}}{=} f_i(\boldsymbol{x},\boldsymbol{y}), \\ \dot{y}_i = -[K_i''(\boldsymbol{x},\boldsymbol{y}) + \alpha U_i''(\boldsymbol{x},\boldsymbol{y})]x_i' \overset{\text{def}}{=} h_i(\boldsymbol{x},\boldsymbol{y}). \end{cases} \tag{45}$$

Runge–Kutta 2 yields the following scheme:

$$\begin{cases} \widetilde{x}_i(t+\Delta t) = x_i + f_i(\boldsymbol{x},\boldsymbol{y})\Delta t, \\ \widetilde{y}_i(t+\Delta t) = y_i + h_i(\boldsymbol{x},\boldsymbol{y})\Delta t, \end{cases}$$
$$\begin{cases} x_i(t+\Delta t) = x_i + \dfrac{f_i(\boldsymbol{x},\boldsymbol{y}) + f_i(\tilde{\boldsymbol{x}},\tilde{\boldsymbol{y}})}{2}\Delta t, \\ y_i(t+\Delta t) = y_i + \dfrac{h_i(\boldsymbol{x},\boldsymbol{y}) + h_i(\tilde{\boldsymbol{x}},\tilde{\boldsymbol{y}})}{2}\Delta t. \end{cases} \tag{46}$$

After each step we rearrange the spline so that the generating points of the new interface are an equally spaced discretization of the new arclength. Therefore, at the beginning of each step, the arclength is the arclength of the initial configuration, and can be treated as a time-independent parameter. The ambiguity with a variable arclength arises in the second sweep of the Runge–Kutta scheme. Indeed, functions $f_i(\tilde{\boldsymbol{x}},\tilde{\boldsymbol{y}})$ and $g_i(\tilde{\boldsymbol{x}},\tilde{\boldsymbol{y}})$ are based on the derivatives of a parameter which is not an arclength any more. Thus, a new metric $g = \sqrt{x'^2 + y'^2}$ should be defined, and formulate for an arbitrary parameter that include this metric should be used. We neglect this fact and assume that the parameter is still the arclength on the second sweep of Runge–Kutta scheme. Strictly speaking, this means that the integration scheme used is not exactly Runge–Kutta 2. It is more accurate than an Euler scheme, but less accurate than a perfect Runge–Kutta 2.

5. Distribution of voltage

The voltage distribution is required only along the interface line, and therefore we use the boundary element approach to avoid discretization of the interior domain. Thus, we deal with a static problem, and the boundary integral reduces the two-dimensional problem to a one-dimensional one. The conductivities of the two grains are assumed equal and constant throughout the grain domains. The intergranular boundary does not contribute additional resistance. The resistance of the void is assumed infinite.

The distribution of the voltage inside a homogeneous medium of constant resistance is described by the Laplace equation with Dirichlet and Neumann boundary conditions

$$\nabla^2 U = 0 \quad \text{or} \quad U_{xx} + U_{yy} = 0. \tag{47}$$

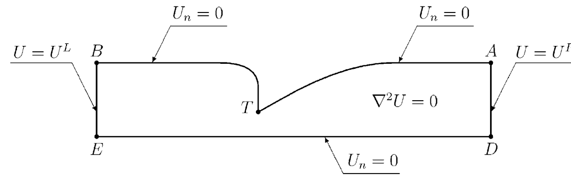

Fig. 6. Boundary conditions for the voltage distribution problem.

The boundary conditions are shown in Fig. 6. Consider the case of an infinite resistance of the void (line exposed to air at its top surface). At the vertical ends of the interconnect, where the electrodes are attached, the value of the potential is set: $U = U^{\mathrm{L}}$ at the left side BE and $U = U^{\mathrm{R}}$ at the right side AD. Along the top side $AT + TB$ and the bottom side DE the normal derivative of voltage vanishes, because the top side contacts with the air and the bottom side is normally attached to a diffusion barrier layer whose conductivity is neglected in this study.

Application of the boundary integral method reduces the Laplace equation to the integral equation

$$U(\xi) = \frac{1}{\pi - \alpha_\xi} \oint \left[\frac{\partial \ln R(\xi, \Gamma)}{\partial n} U(\Gamma) - U_n(\Gamma) \ln R(\xi, \Gamma) \right] \mathrm{d}\Gamma, \tag{48}$$

where ξ is a given fixed point of the boundary; $\alpha_\xi = 0$ if the boundary is smooth at that point, and $\alpha_\xi = \alpha^+ - \alpha^-$ is the change in the direction of the tangent line if there is a sharp angle. Positive values of α_ξ correspond to a locally sharply convex shape of the domain, and negative values correspond to a sharply concave shape. $R(\Gamma, \xi)$ is the radius vector from the given fixed point ξ on the boundary to a 'running' point Γ of the boundary under the sign of integral, as shown in Fig. 7. $\partial/\partial n$ denotes the derivative in the direction of the outward normal to the boundary at that point Γ; $U(\Gamma)$ is the voltage at the 'running' point, and $U_n(\Gamma)$ is its normal derivative.

Discretization of the boundary assumes that the voltage and its derivative accept definite values at the nodes. For a medium of homogeneous resistance, either the voltage U, or its normal derivative U_n is specified at each point of the boundary. An interpolation function is assumed between the nodes; in this work we applied a linear interpolation. Continuous linear elements with the nodes at the ends of the element are used. Thus, it is assumed that the voltage and its normal derivative have a linear evolution along the elements, except at the points with sharp angles, where the derivative may jump. The curvilinear grain–void interface is approximated by segments of a straight line. Formally, this leads to sharp angles at the joints. However, since the original boundary is smooth and the 'sharpness' is very small, no jump of the derivative is assumed at these nodes. The discontinuity of the normal derivative is allowed only at the triple point T and at the right angles A, B, D and E (Fig. 7). At these right angles, $\alpha_\xi = +\pi/2$, and at the triple point α_ξ is negative and equal to $2\theta - \pi$.

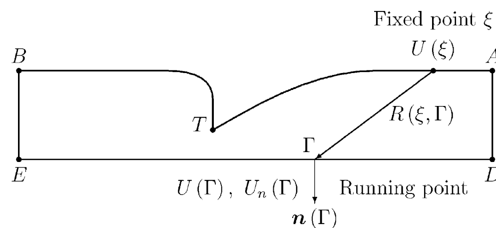

Fig. 7. Illustration for boundary integral equation.

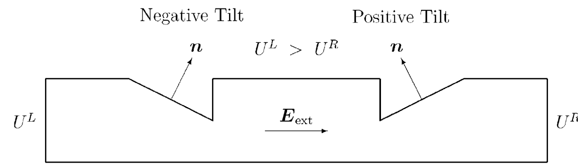

Fig. 8. Positive and negative tilt of grain–void interface.

The interpolation makes it possible to replace the integrals by sums, and the integral equation (48) becomes a linear set. Its solution yields the values of the voltage where the voltage derivative was initially specified, and the values of the derivative where the voltage was set. In particular, we establish the voltage U at each node of the curvilinear grain–void interface, and then approximate its second derivative U_{ss} with respect to the arclength, applying the central differences. At the triple point, backward and forward differences are applied for the right and left branches, respectively. In this study, we followed the methodology of the boundary element method described by Paris and Canas in [6] and used the codes supplied with this book.

Once the unknown grid values of the voltage derivative U_n are established along the vertical sides of the interconnect DA and BE, its estimated total resistance becomes

$$R = \frac{U^{\mathrm{L}} - U^{\mathrm{R}}}{k_{\mathrm{g}} \int_h U_n \, \mathrm{d}\Gamma}, \tag{49}$$

where k_{g} is the specific electric conductivity of the grain material, $U^{\mathrm{L}} - U^{\mathrm{R}}$ is the external voltage applied to the interconnect, and h is the path of integration. We assume $k_{\mathrm{g}} = 1$. Either the left or the right vertical side of the interconnect can be used as the path h. The result is the same up to the sign, since the circulation of the normal derivative around the contour of the interconnect vanishes

$$\oint U_n \, \mathrm{d}s = 0. \tag{50}$$

This is a property of the solution of the Laplace equation. Since along the top and bottom sides of the interconnect U_n vanishes due to the boundary conditions

$$\int_{BE} U_n \, \mathrm{d}\Gamma = -\int_{DA} U_n \, \mathrm{d}\Gamma. \tag{51}$$

We use the path $h = BE$ in Eq. (49) in order to obtain the positive value of the resistance.

The resistance varies as the front evolves and it is independent of the applied voltage, since the field problem is linear. We use Ohm's law to calculate the resistance.

6. Numerical simulation

The interface evolution under surface diffusion and electric field forces was examined numerically for different ratios between diffusion and electric field forces, and for different initial configurations of the grain–void interface. Results of two sets of simulations are presented below. The first set displays interface motion of a single grain–void interface. The second set presents the interface dynamics of a two-grain bamboo sector.

The 'bottleneck' of the numerical simulations is the electrostatic problem of voltage distribution. The boundary element formulation of the Laplace equation with mixed boundary conditions leads to a small

but fully populated matrix (400–500 degrees of freedom is a typical number). Since the small time step is dictated by a stability threshold for the fourth-order equation, we can update the voltage distribution not every time step, but once every several steps without significant loss of accuracy. Actually, we update the voltage distribution adaptively. At the beginning of the simulations, the changes in shape are rapid, and we update the electric field each step and even each swap of Runge–Kutta. Then we do it periodically. We discovered, however, that when we update the field once per few thousand steps, this causes not only a loss of accuracy, but also a numerical instability that occurs even when changes in the interface configuration are still pretty small.

Note that we pass the bamboo contour clockwise, and thus we pass its upper interface line from the right to the left. The graphs for curvature, voltage and their derivatives are plotted vs arclength s. The initial point A at $s = 0$ corresponds to the right end of the interface line, and the final point B at $s = S_{\max}$ corresponds to its left end.

In all simulations, the top interface line includes 200 intervals. There are 50 intervals for each vertical side and 100 intervals for the bottom side. There are 400 nodes total for the boundary element discretization. The bamboo line length is 12 normalized dimensionless units, and the external voltage drop is also 12, so that the external electric field has a unit strength. The nominal width of the line is 2. The ratios between the field and diffusion forces are $\alpha = 10$ or $\alpha = 20$. In the plots we specify the length of the curved interface S, and the absolute change in area of the interconnect A (due to small numerical errors). The nominal area of the interconnect is 24, except for the case with tilted bamboo line (Fig. 10), where the nominal area is 22. We display also the physical normalized 'problem time' P_t and the resistance R. A change in resistance may be used as a performance criterion for the interconnect.

6.1. Evolution of a bamboo interface with no initial irregularities

Consider a bamboo line of a plain rectangular initial shape with no irregularities. Initially the grain–void interface AB is parallel to the direction of the applied external electric field at any point. The boundary conditions at the electrode points are described by Eq. (5). Initially the distribution of voltage along such line is linear, and the voltage gradient along the grain–void interface is constant and equal to the strength of the external electric field. In our frame of reference, the arclength increases from the right to the left, and therefore

$$U_s^A = U_s^B = E_{\text{ext}} = \frac{U^B - U^A}{L_x}. \tag{52}$$

We assume that a higher potential is applied at the left electrode B, so that the external field and the arclength derivatives of voltage at the electrode points are positive. Since, according to Eq. (5), the flux at the electrode points vanishes, the derivatives of curvature are negative

$$K_s^A = K_s^B = -\alpha E_{\text{ext}}. \tag{53}$$

Initially the interface line is straight, and its curvature vanishes everywhere. This means that at all other points, except the electrodes, the derivative of curvature is zero. Now consider the second derivatives of curvature at the electrode points. When we approach the right electrode end from the left side (i.e., in the direction opposite to the direction of increasing arclength), the derivative of curvature changes from zero to a negative value, i.e., decreases. The same happens when we approach the left electrode point from the right side (in the direction of increasing arclength). This means that the second derivative of curvature is negative at the left electrode and positive at the right

$$K^A_{ss} > 0, \quad K^B_{ss} < 0. \tag{54}$$

Since at $t = 0$ the voltage changes linearly along the line, its second derivative is zero, and at the initial moment, the interface velocity includes formally the diffusion component only. The magnitude of this component, however, is governed by the applied voltage. The void decreases at the left end, and increases at the right. At the initial instance, the picture is fully skew-symmetric, and the interface velocities have equal magnitudes and opposite signs. Later the symmetry is violated, but the tendency remains: there is an accumulation of metal at the anode B and depletion of the material at the cathode A. The results of a numerical simulation for a plain bamboo line are presented in Fig. 9 for a weak field $\alpha = 10$ and for a moderate field $\alpha = 20$. After some time, the thickness of the interconnect line near the cathode becomes

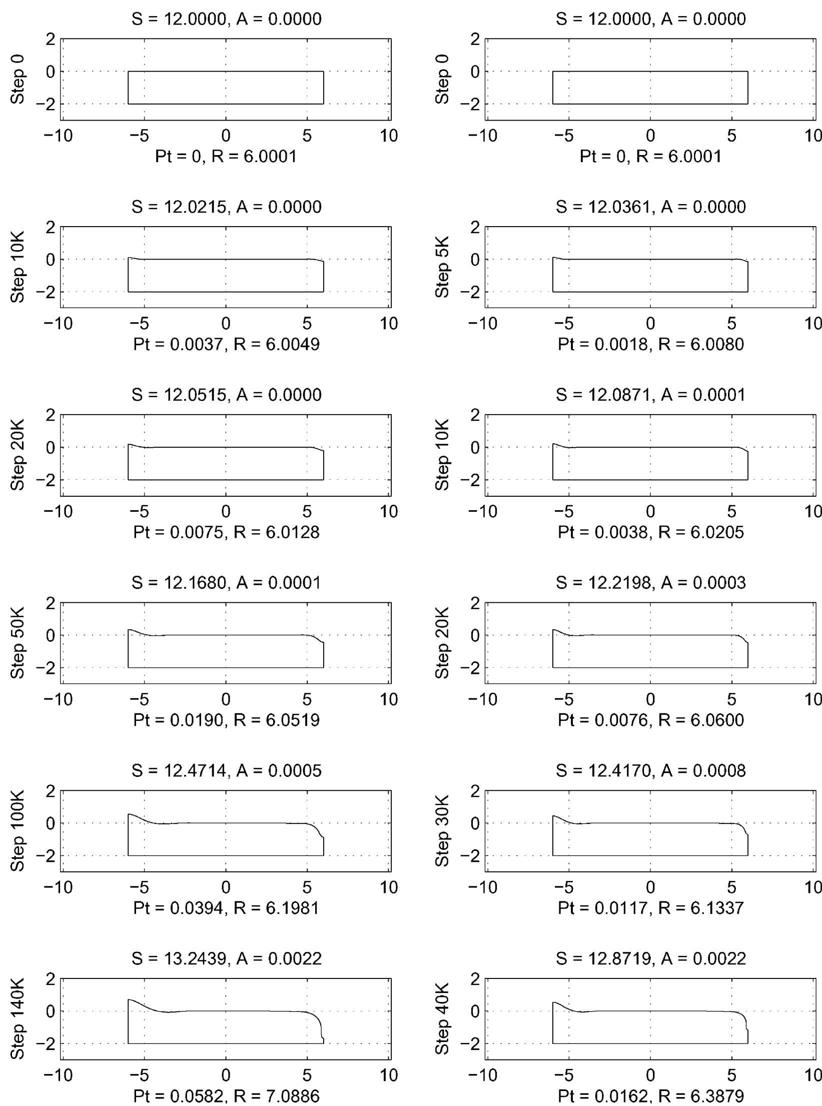

Fig. 9. Evolution of a plain top interface line with no initial irregularities, $\alpha = 10$ (left column) and $\alpha = 20$ (right column).

zero, and an open circuit failure occurs. These results are qualitatively confirmed by Liniger et al. [59], who investigated the change of linewidth near the electrodes with the scanning electron microscope and discovered a very similar scenario at the cathode and the anode regions of the metal line. Depletion of aluminum near the cathode was also studied by Suo [37].

6.2. Evolution of a bamboo interface with initial tilt

In Fig. 10 we consider an initial configuration with special irregularities: triangular faceted voids with positive and negative tilts with respect to the external electric field. Graphs for curvature and voltage and

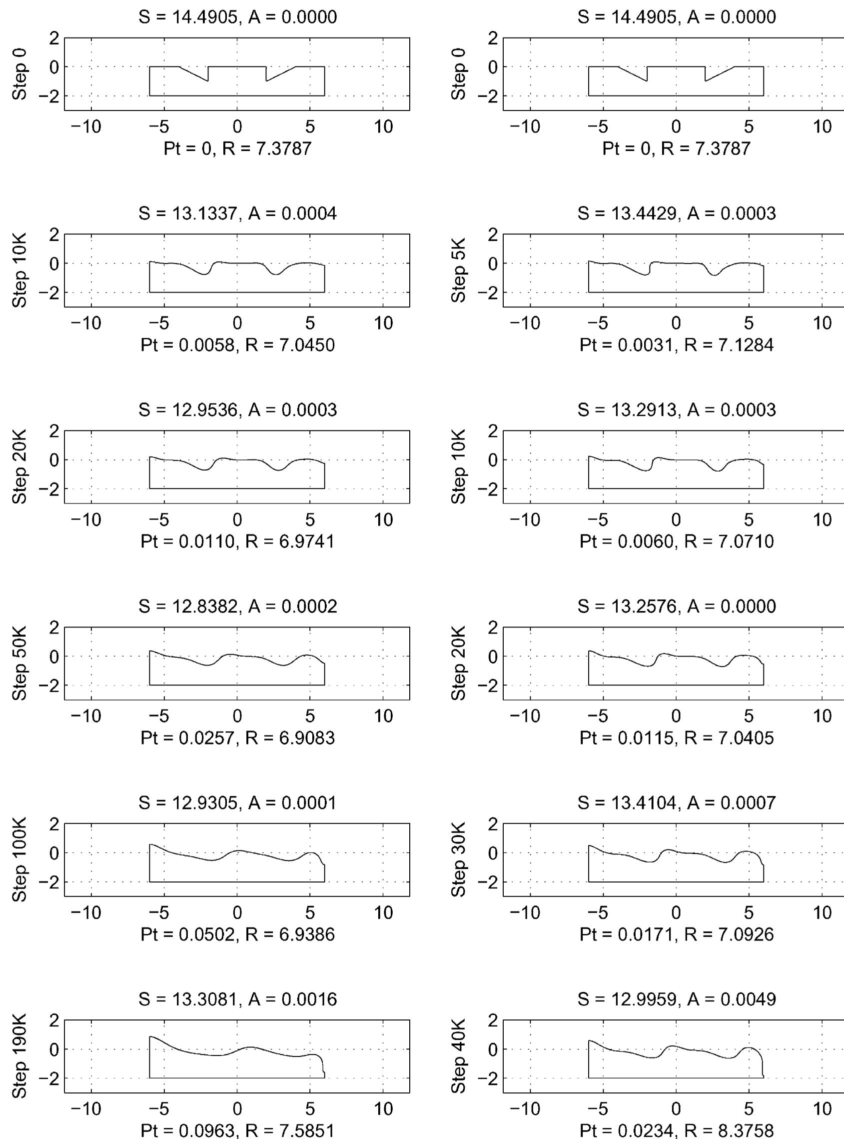

Fig. 10. Evolution of the top interface line for a bamboo line with initial tilts, $\alpha = 10$ (left column) and $\alpha = 20$ (right column).

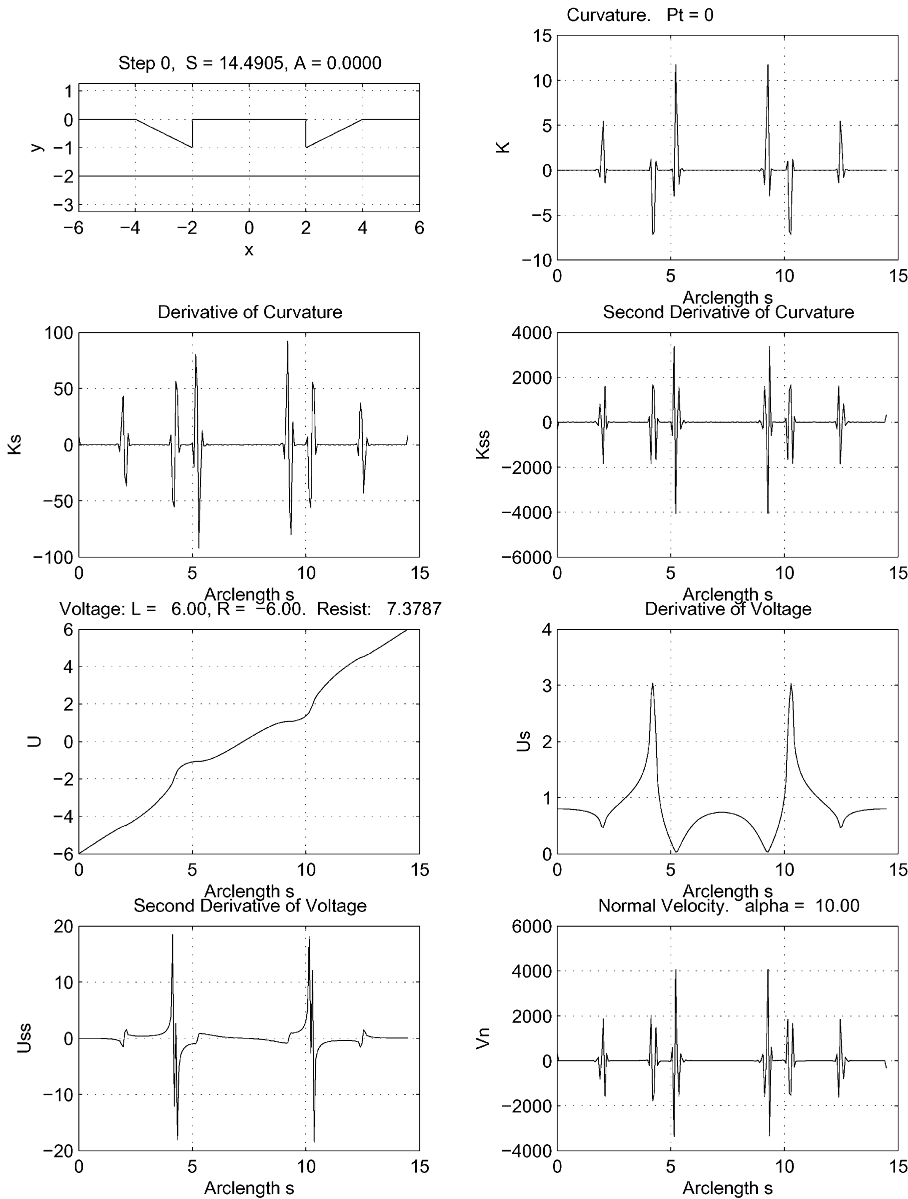

Fig. 11. Curvature and voltage distributions for a bamboo line with initial tilts.

their derivatives with respect to arclength are shown for the initial configuration of the grain–void interface in Fig. 11. The same graphs after 1.9×10^5 time steps are plotted in Fig. 12. The initial tilt angles for the bamboo line presented in Fig. 10 are $\arctan 1/2$.

Let $\boldsymbol{E}$ be the external electric field, and $\boldsymbol{n}$ be the outward normal to the tilted surface of the bamboo line. We follow the notations accepted in the literature [27,49] and define the positive tilt as one with $\boldsymbol{E} \cdot \boldsymbol{n} < 0$; for the negative tilt this scalar product is positive, as illustrated in Fig. 8.

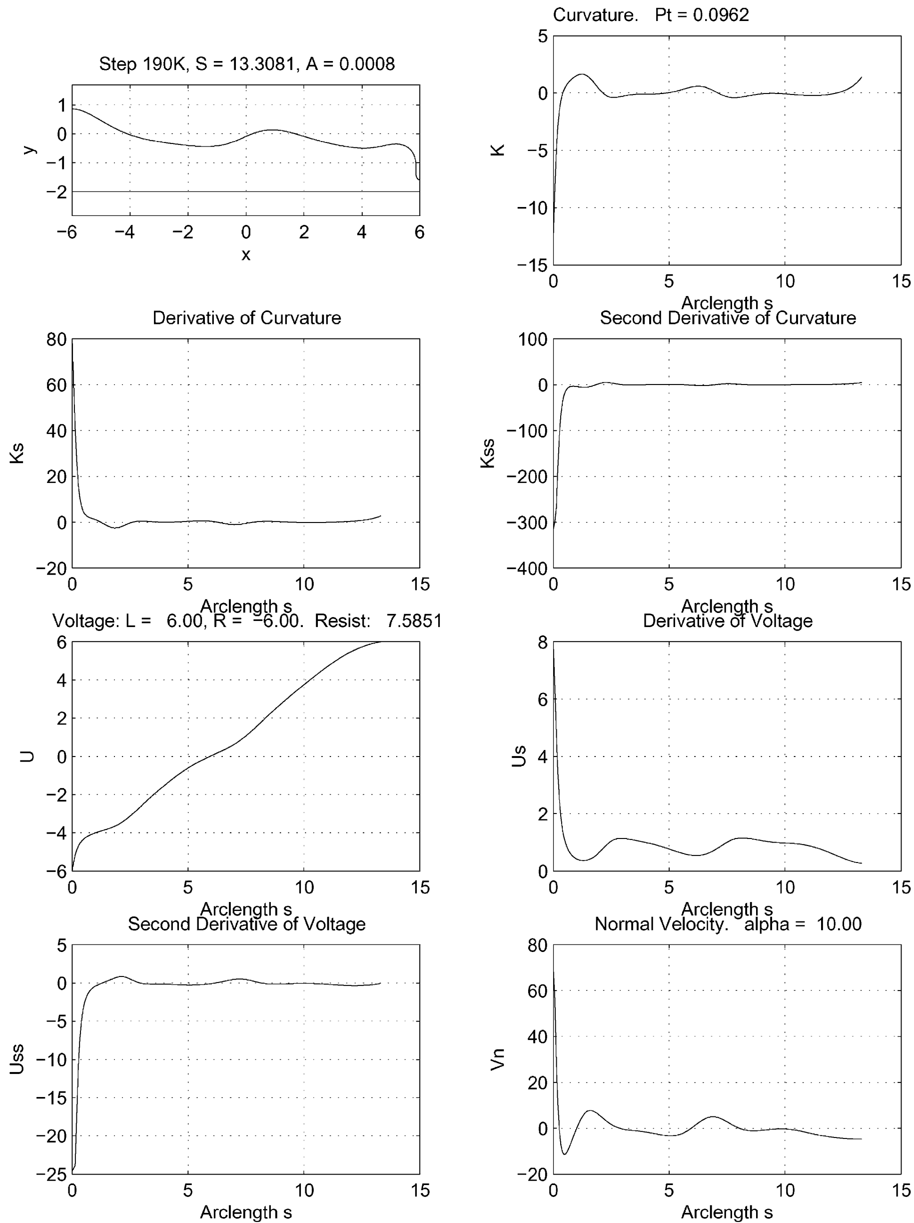

Fig. 12. Curvature and voltage distributions for a bamboo line with initial tilts after 1.9×10^5 time steps.

Subplots of Fig. 10 show the bamboo contour after the specified numbers of steps. One can see from these plots that the negative tilt is stable in evolution, while the positive tilt is unstable. These results are in agreement with experimental studies of Kraft et al. [50], where the behavior of electromigration-induced voids in narrow unpassivated aluminum interconnects was examined using scanning electron microscopy. Our numerical results coincide also with those obtained analytically by Maroudas [27,49] and Gungor and Maroudas [13]. Maroudas [49] studied the electromigration of bamboo lines with positive and negative tilts,

applying the linear stability theory. He considered the small amplitude perturbation of the void surface shape about the planar facet morphology, and proved theoretically that only lines with negative tilt are stable. The tangential component of the external electric field $E_s = E\cos\theta$ was used to approximate the derivative of voltage along the void-interface line for a facet tilted by angle θ with respect to the far field E_∞. In [13], Gungor and Maroudas applied a full numerical simulation to solve two coupled differential equations: Laplace's equation (with the boundary element approach) for the computation of the electric field distribution, and the continuity equation for surface transport, and compared the results with the linear stability theory.

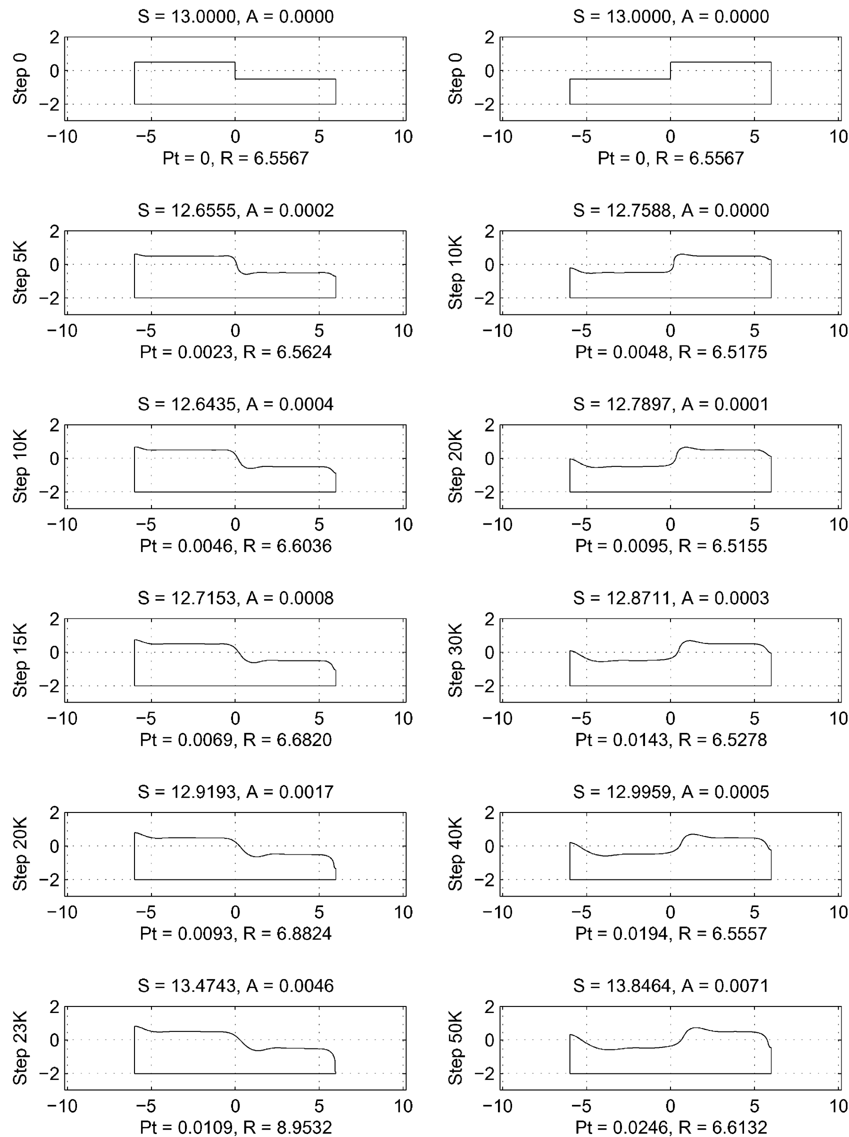

Fig. 13. Evolution of a bamboo interface line with an initial 'step', $\alpha = 20$.

6.3. Evolution of a bamboo interface with an initial 'step'

The evolution of a stepped contour with field lines entering or exiting the 'step' is shown in Fig. 13. The ratio of the field forces to the diffusion forces $\alpha = 20$. A 'step' may be considered as an ultimate case of a tilted contour, with a normal (positive or negative) tilt. For a positive 'step', the field direction coincides with the outward normal to the step line, and for a negative 'step' these directions are opposite. We run the simulations until the thickness of the line near the cathode became zero (and the resistance of the interconnect becomes infinite). The line with a negative step had a lesser initial thickness near the cathode, and thus its life is shorter.

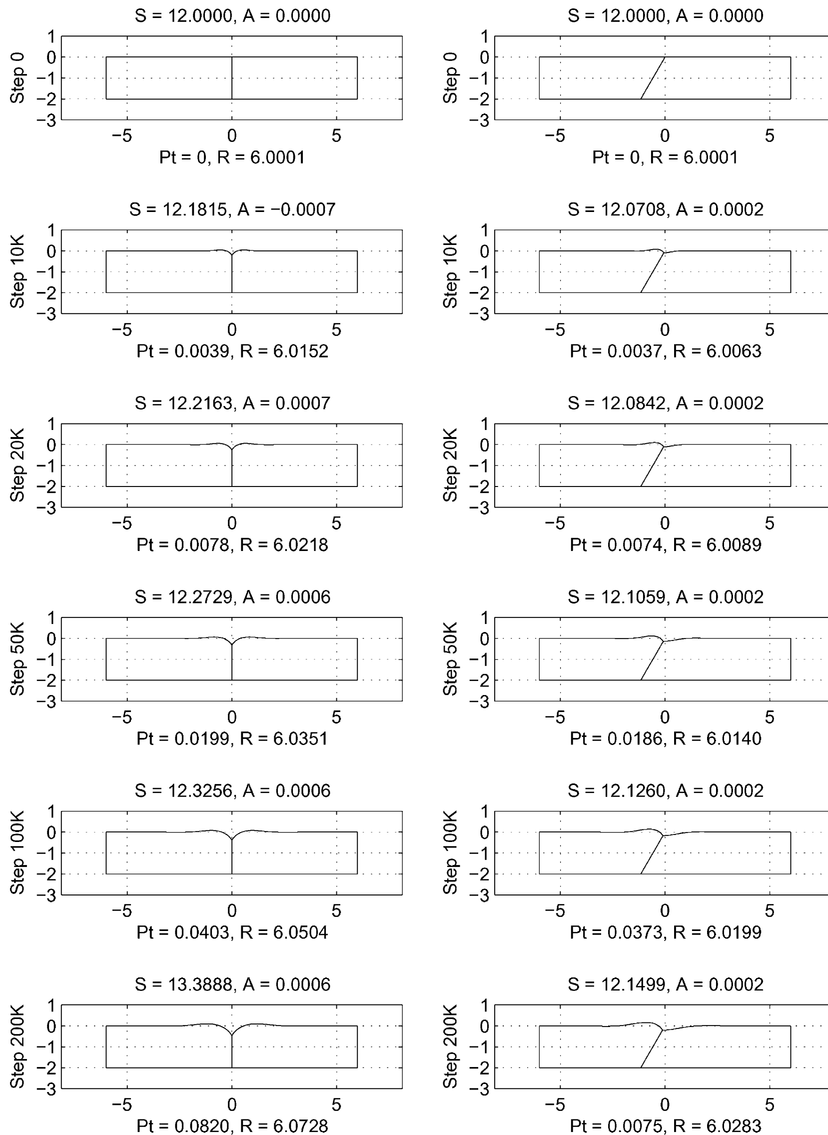

Fig. 14. Two-grain void-interface motion under diffusion forces: $\alpha = 0$, $\beta = \pi/2$ (left column) and $\alpha = 0$, $\beta = \pi/3$ (right column).

6.4. Evolution of a two-grain bamboo section

Next we study a number of modifications of the classical Mullins problem of thermal grooving [46–48]. We consider a two-grain Mullins problem with a normal and tilted boundary between the grains, examining positive and negative tilts. Each branch of the curved interface – right and left (i.e., related to grains 1 and 2, respectively) includes 100 intervals. Each vertical side includes 50 intervals, and the bottom side includes 100 intervals, for a total of 400 nodes. The interconnect length and the external voltage are the same as for single-grain simulations. Angles between the void-interface contours and the intergranular boundary are $\theta = \pi/6$ for all cases (for both normal and tilted intergranular boundaries).

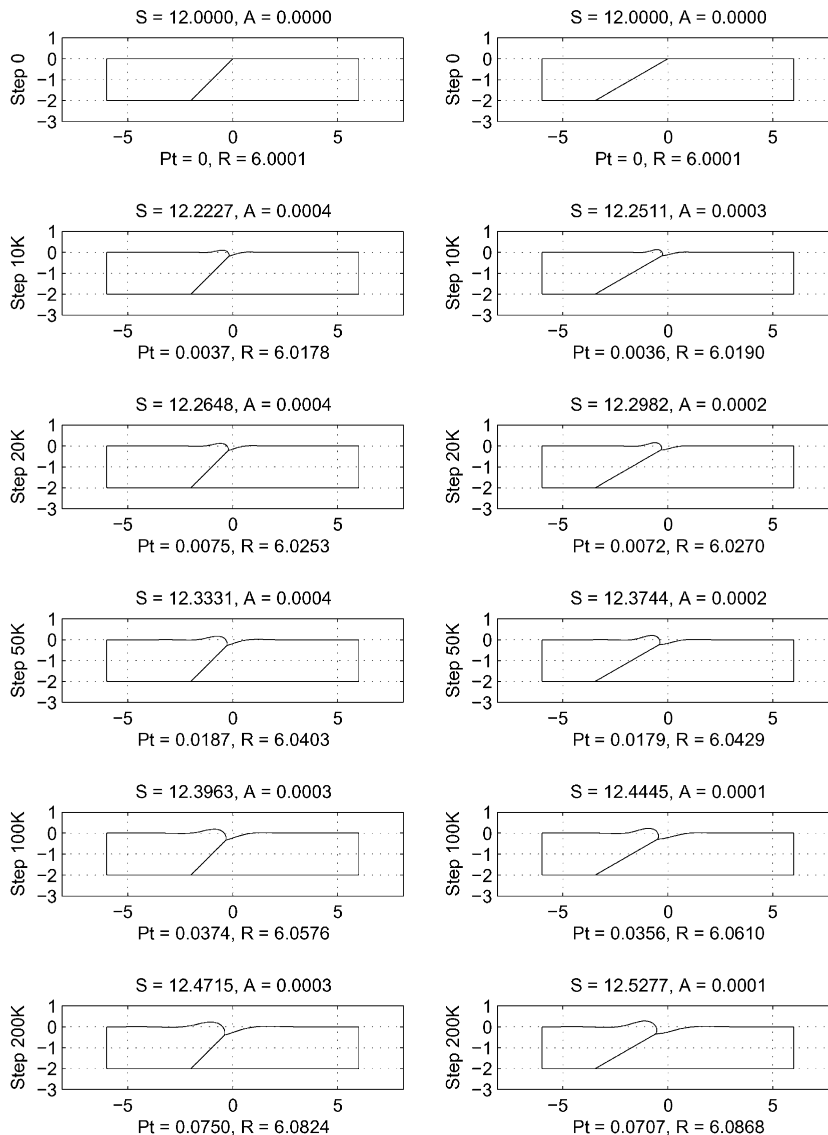

Fig. 15. Motion under diffusion forces: $\alpha = 0$, $\beta = \pi/4$ (left column) and $\alpha = 0$, $\beta = \pi/6$ (right column).

Motion under surface diffusion only is shown in Figs. 14 and 15. Fig. 14 shows the evolution of a two-grain section of a bamboo line: in the left column with a normal boundary between the lines ($\beta = \pi/2$, classical Mullins problem), and in the right column with a slightly tilted boundary ($\beta = \pi/3$). Fig. 15 shows the motion under diffusion only for a moderate tilt ($\beta = \pi/4$, left column) and a large tilt ($\beta = \pi/6$, left column). Recall that β is the angle between the external electric field and the vector of the intergranular boundary. The intergranular boundary is considered directed outward of the material at the triple point. In the absence of an

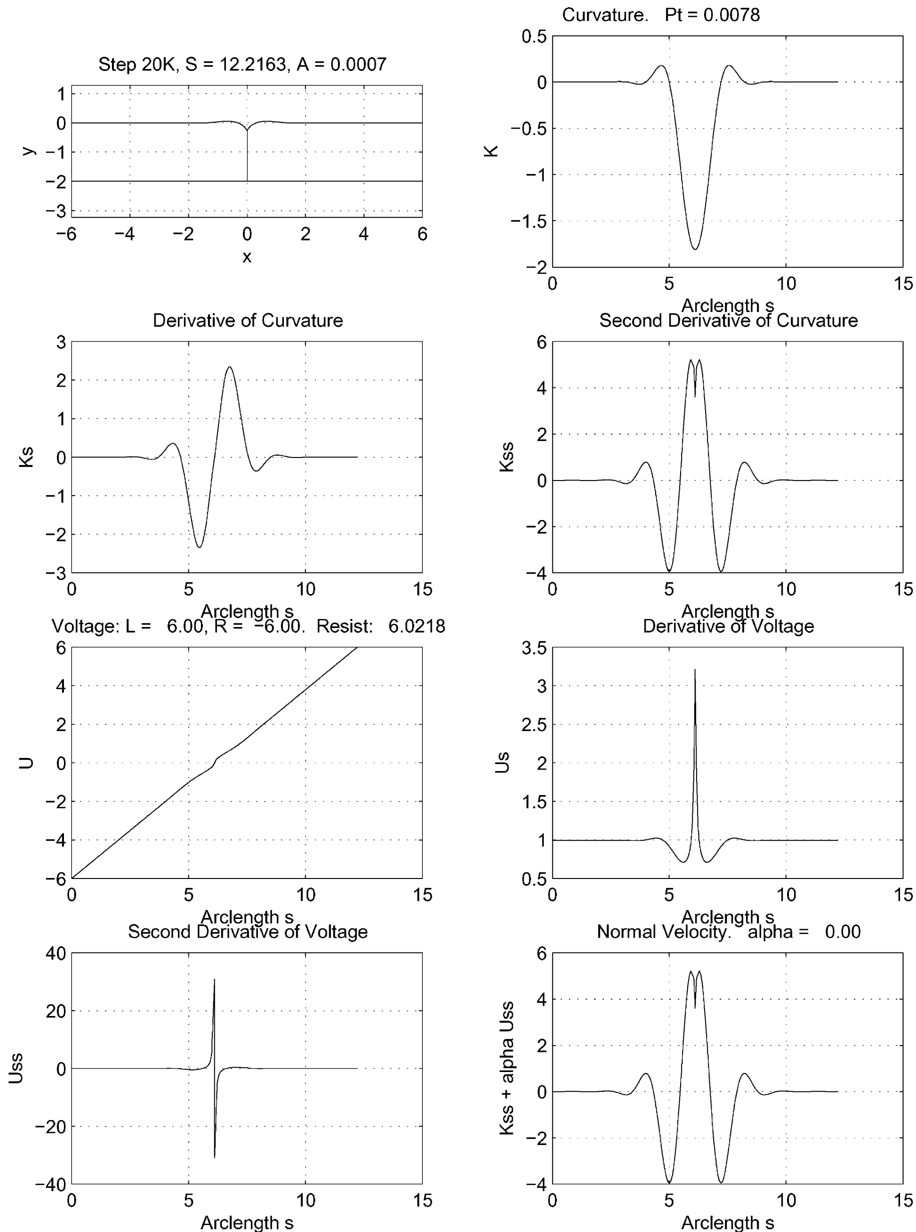

Fig. 16. Motion under diffusion forces: distribution of curvature and voltage after 20,000 steps. $\alpha = 0$, $\beta = \pi/2$.

electric field, β is the angle between the intergranular boundary and the positive x-axis (horizontal side of the interconnect). Obtuse angles $\beta > \pi/2$ are not considered, because in the absence of the field they give symmetric results with respect to acute angles $\pi - \beta$. 2×10^5 time steps were run.

Fig. 16 shows the distribution of curvature, voltage and their derivatives vs. interface arclength for $\alpha = 0$, $\beta = \pi/2$ after 2×10^4 steps. Although the voltage does not affect the interface motion, its distribution is still established and plotted for reference.

Interface evolution under diffusion and field forces for a normal intergranular boundary is presented in Fig. 17. Motion in the weak field $\alpha = 10$ is presented in the left column, and motion in the moderate field $\alpha = 20$ in the right column.

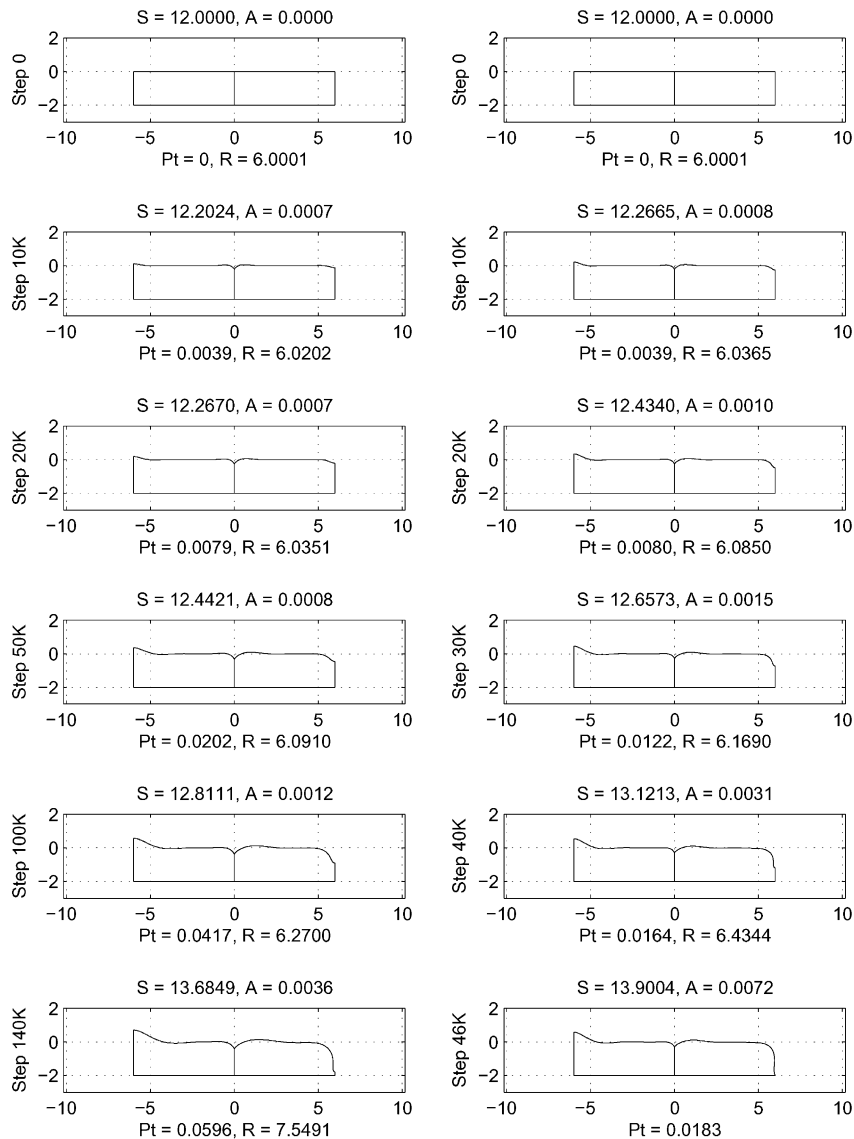

Fig. 17. Motion of a system with a normal intergranular boundary under diffusion and electric field forces: $\alpha = 10$, $\beta = \pi/2$ (left column) and $\alpha = 20$, $\beta = \pi/2$ (right column).

Comparing results in Fig. 14 with those in Fig. 17, we conclude that under diffusion forces alone, the groove between two grains becomes deeper and thus more dangerous than under the action of both diffusion and electric field. One may say that the field has a balancing, stabilizing effect at the triple point. The stabilizing ("healing") effect of the electric field is illustrated in Fig. 18. This figure shows the configuration of the interconnect and graphs for curvature and voltage after 10^4 time steps for $\alpha = 20$ and $\beta = \pi/2$. Consider plots for the second derivative of curvature K_{ss} and the second derivative of voltage U_{ss}, both with respect to arclength, in the proximity of the triple point. Both graphs look like a δ-function of a high order,

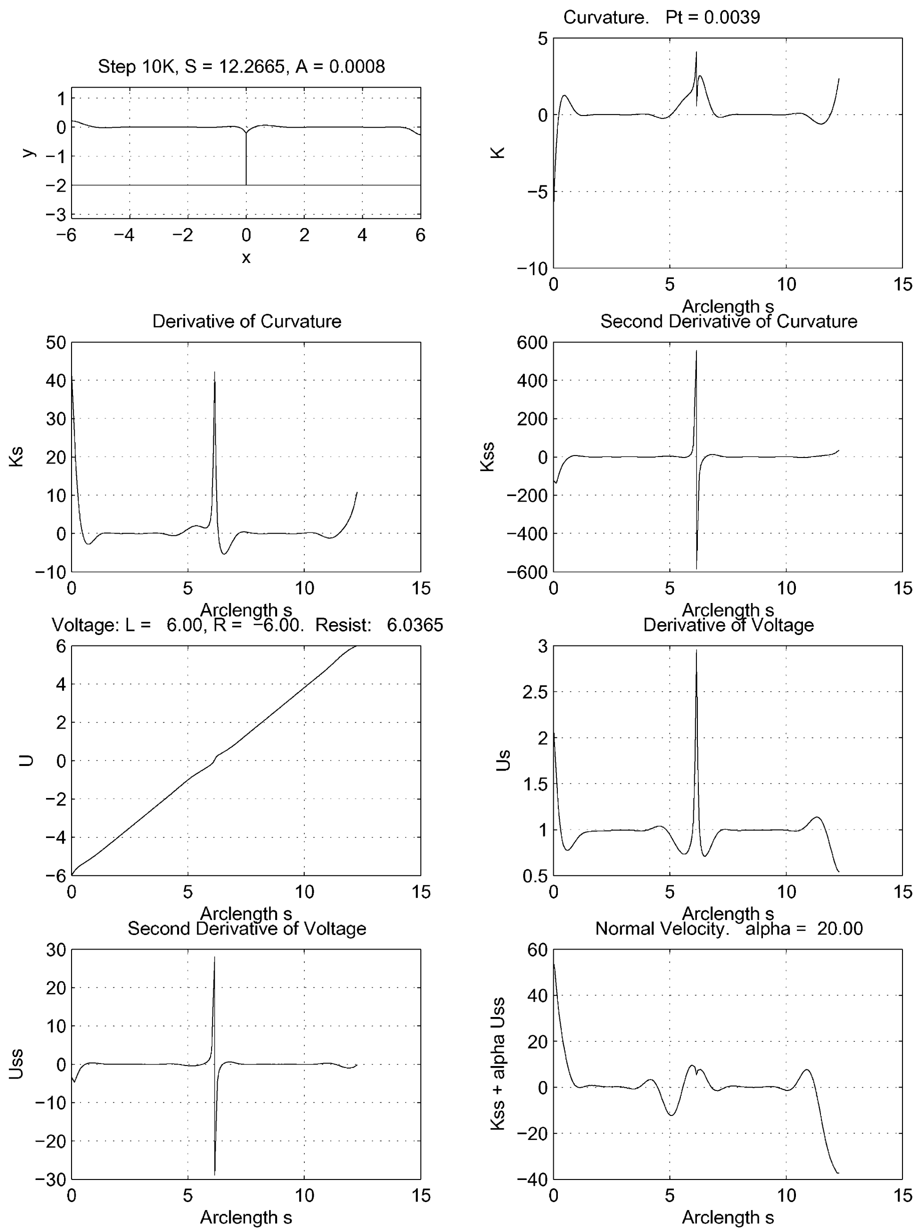

Fig. 18. The stabilizing effect of an electric field: $\alpha = 20$ and $\beta = \pi/2$.

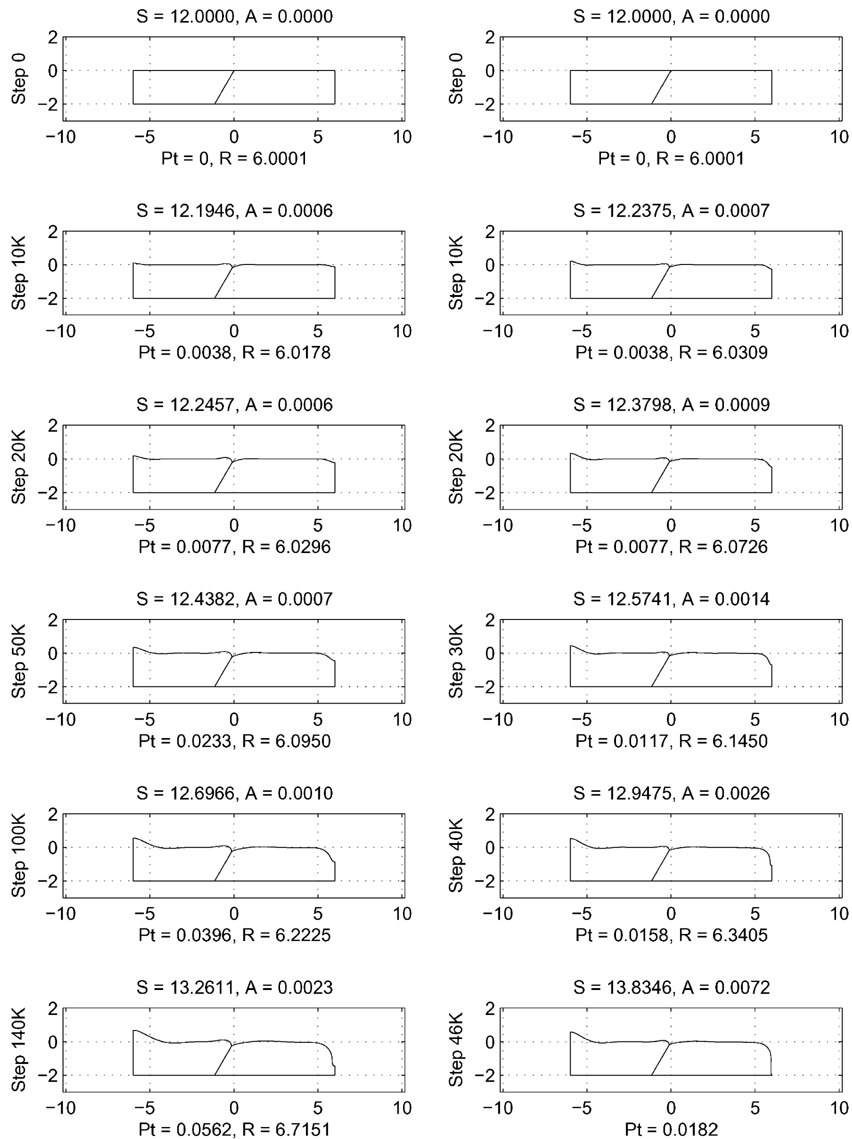

Fig. 19. Two-grain problem with a slightly positively tilted intergranular boundary in a weak and moderate electric field: $\alpha = 10$, $\beta = \pi/3$ (left column) and $\alpha = 20$, $\beta = \pi/3$ (right column).

but these two δ-functions have opposite signs. As we see from the graph for the normal velocity F, their linear combination $F = K_{ss} + \alpha U_{ss}$ has much less sharper peaks. Positive and negative δ-functions mostly compensate each other. A similar effect is seen in Fig. 25.

The dynamics of the two-grain system with a tilted intergranular boundary are presented in the numerical simulations below. We define the tilt as positive for $0 < \beta < \pi/2$ and negative for $\pi/2 < \beta < \pi$. In the presence of an electric field, solutions for β and $\pi - \beta$ are not symmetric any more. They are just different solutions. Tilts $\pi/3$ and $2\pi/3$ are considered small, $\pi/4$ and $3\pi/4$ – moderate, and $\pi/6$ and $5\pi/6$ – large.

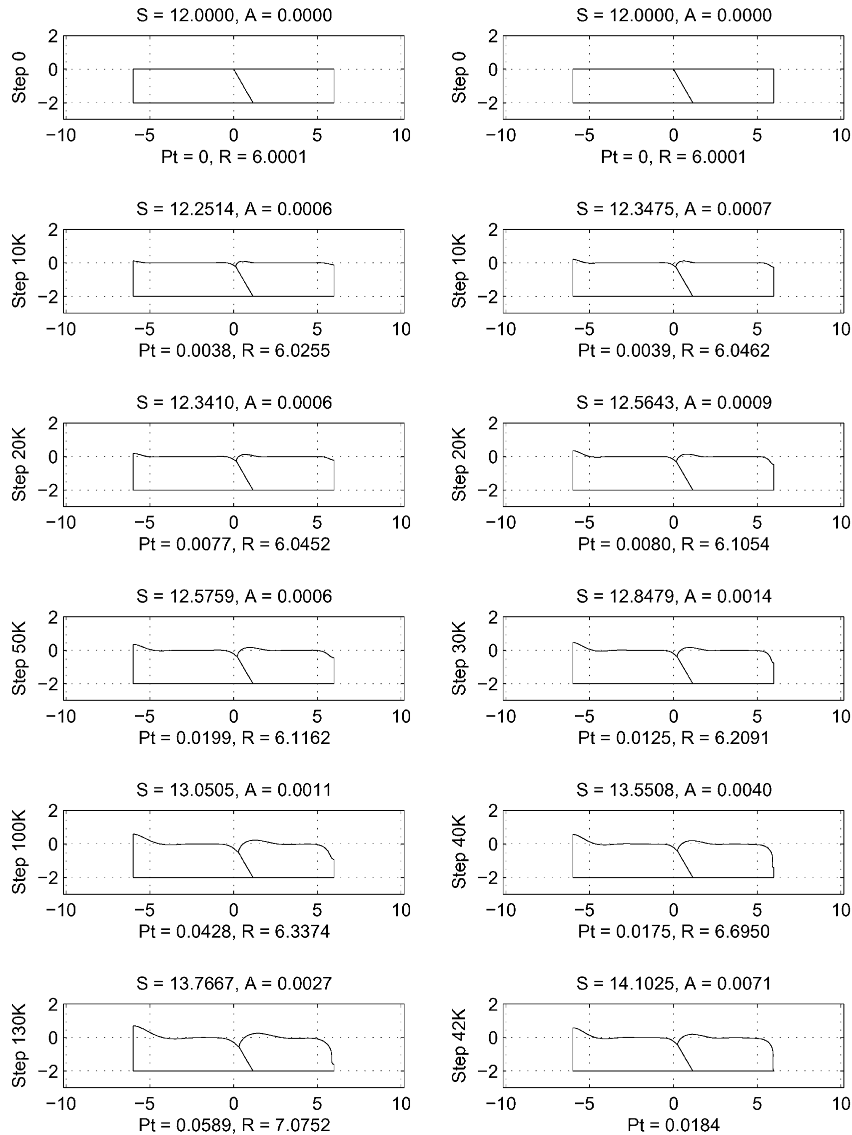

Fig. 20. Two-grain problem with a slightly negatively tilted intergranular boundary in a weak and moderate electric field: $\alpha = 10$, $\beta = 2\pi/3$ (left column) and $\alpha = 20$, $\beta = 2\pi/3$ (right column).

The dynamics of the system with a slightly tilted intergranular boundary are presented in Figs. 19 and 20 for weak and moderate electric fields, respectively, with $\alpha = 10$ and $\alpha = 20$.

The dynamics of the system with a moderately positively tilted intergranular boundary are presented in Figs. 21 and 22 for weak and moderate electric fields, respectively, with $\alpha = 10$ and $\alpha = 20$.

The dynamics of the system with a highly tilted intergranular boundary are presented in Figs. 23 and 24 for weak and moderate electric fields, respectively, with $\alpha = 10$ and $\alpha = 20$.

The distribution of the curvature and voltage for the system with $\alpha = 20$ and $\beta = 5\pi/6$ after 4×10^4 time steps is presented in Fig. 25.

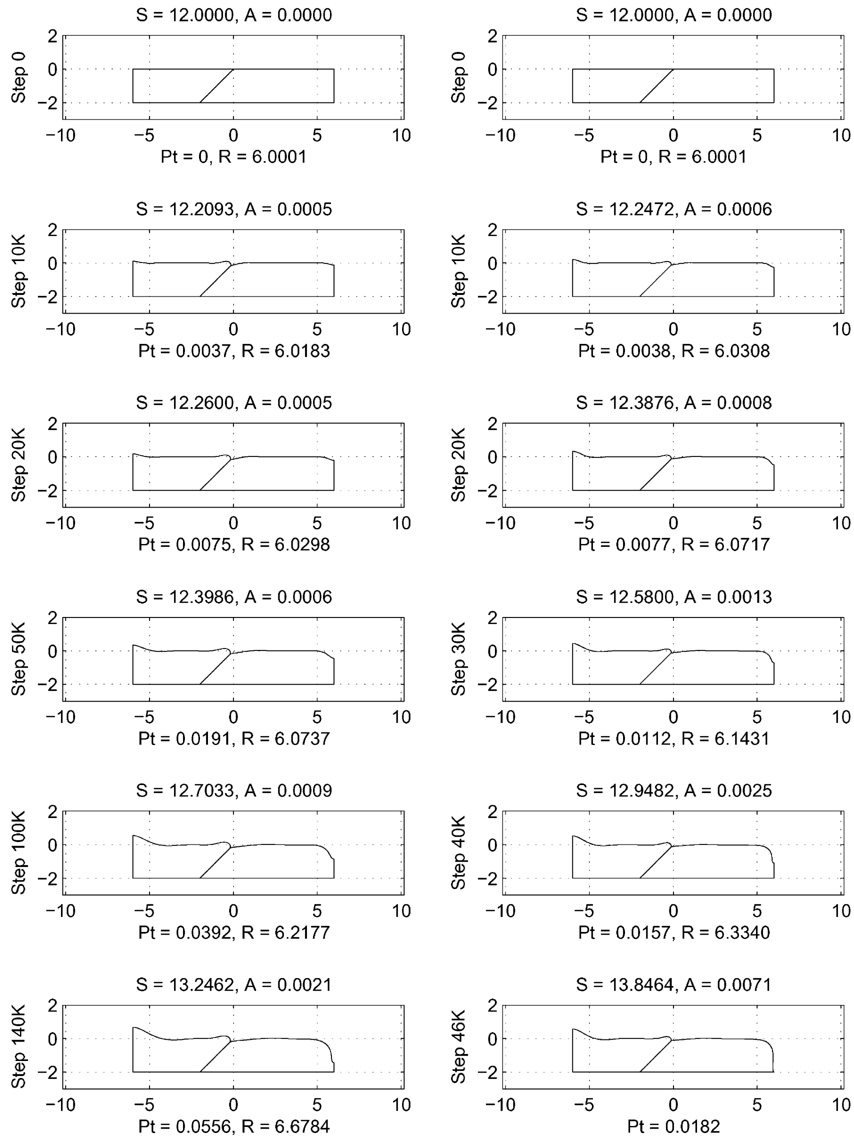

Fig. 21. Two-grain problem with a moderately positively tilted intergranular boundary in weak and moderate electric field: $\alpha = 10$, $\beta = \pi/4$ (left column) and $\alpha = 20$, $\beta = \pi/4$ (right column).

7. Closing remarks

A computational methodology was developed and tested for the simulation of grain–void interface dynamics in bamboo-type interconnects of microelectronic circuits. The motion of the interface under surface diffusion and electric field forces was studied. The resistance of the substrate was assumed infinite.

A finite difference discretization in space and a Runge–Kutta 2 procedure in time were applied in order to solve a set of two coupled fourth-order governing PDEs. The low order of the Runge–Kutta scheme is justified, since the value of the time step is kept fairly small to satisfy stability requirements. The initial

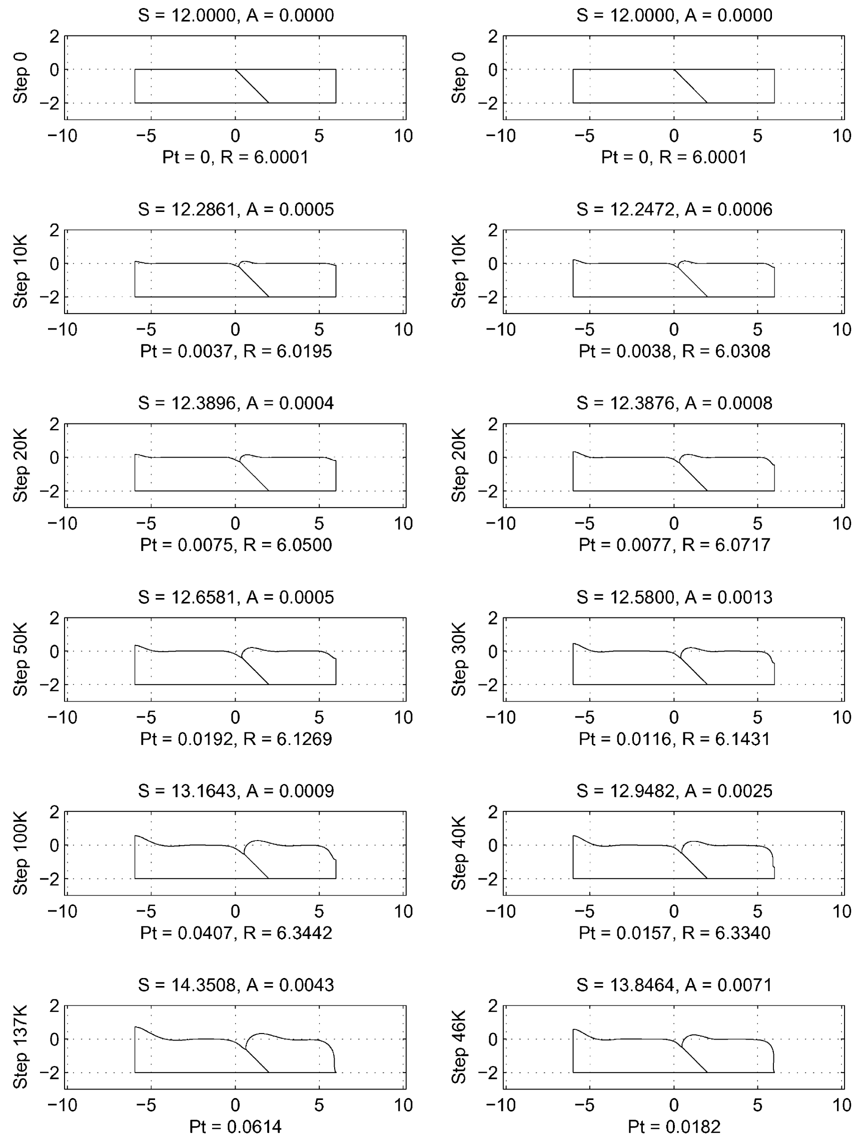

Fig. 22. Two-grain problem with a moderately negatively tilted intergranular boundary in a weak and moderate electric field: $\alpha = 10$, $\beta = 3\pi/4$ (left column) and $\alpha = 20$, $\beta = 3\pi/4$ (right column).

location of the front has to be specified for the governing time-dependent PDEs. In our model, the boundary conditions include vanishing fluxes at the electrode points, and continuity of both flux and velocity of the moving interface at the triple point. The slopes of the interface line are set at the electrodes and at the triple point.

It cannot be denied that the two-dimensional level set method is a more general approach, and gives solutions for more sophisticated electromigration topologies than the one-dimensional formulation applied in this study. However, for the specific problem considered here, the Cartesian formulation becomes an effective and attractive alternative. In particular, we get the solution immediately at the generating points of

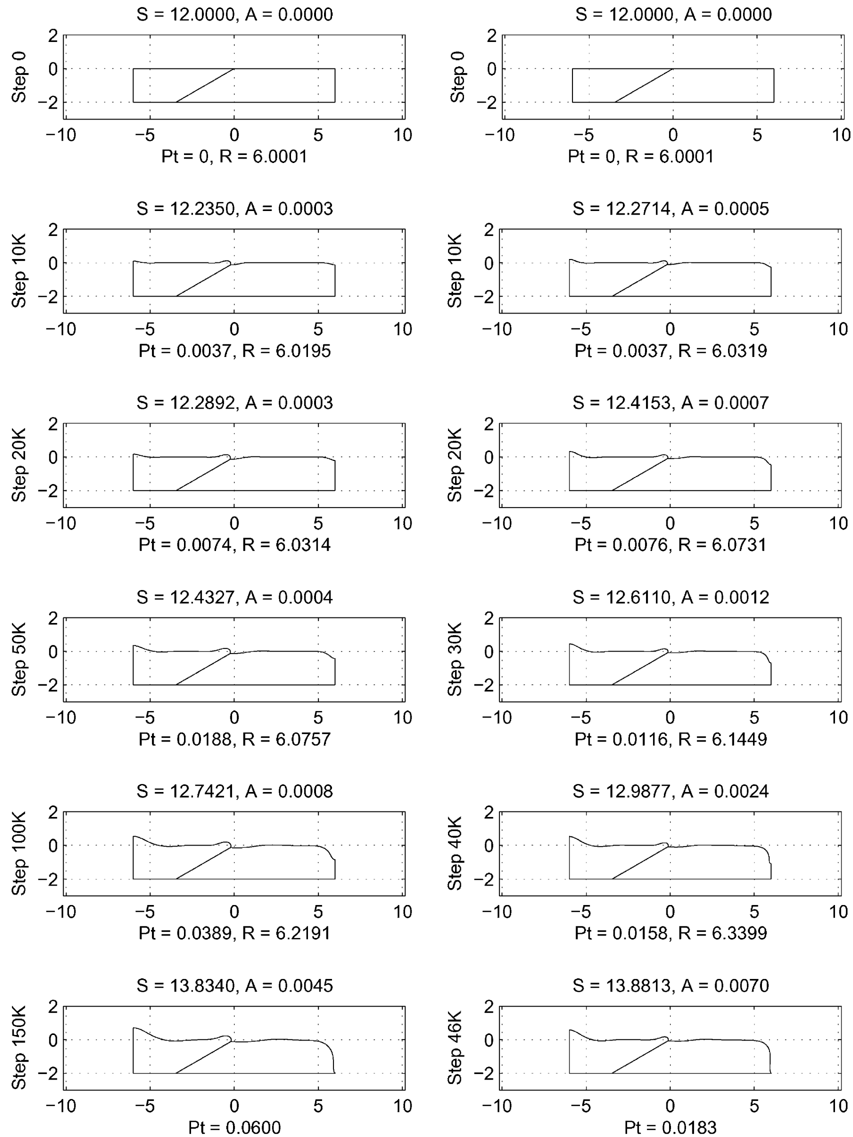

Fig. 23. Two-grain problem with a highly positively tilted intergranular boundary in a weak and moderate electric field: $\alpha = 10$, $\beta = \pi/6$ (left column) and $\alpha = 20$, $\beta = \pi/6$ (right column).

the interface line, and need not apply a two-dimensional interpolation in space to update the location of the interface. Thus, the interpolation error is avoided.

The boundary element method was applied to solve the Laplace equation for the voltage distribution. This method is especially convenient for the curvilinear boundary, since we need the potential values only on the contour line. The variation of the total resistance of the interconnect with time was examined. This value can be further used as an interconnect failure criterion. The electrostatic problem is the 'bottleneck' of the numerical simulation, and consumes most of the computational time, because the resolving matrix of the boundary element formulation is dense. In this study we applied the Gauss

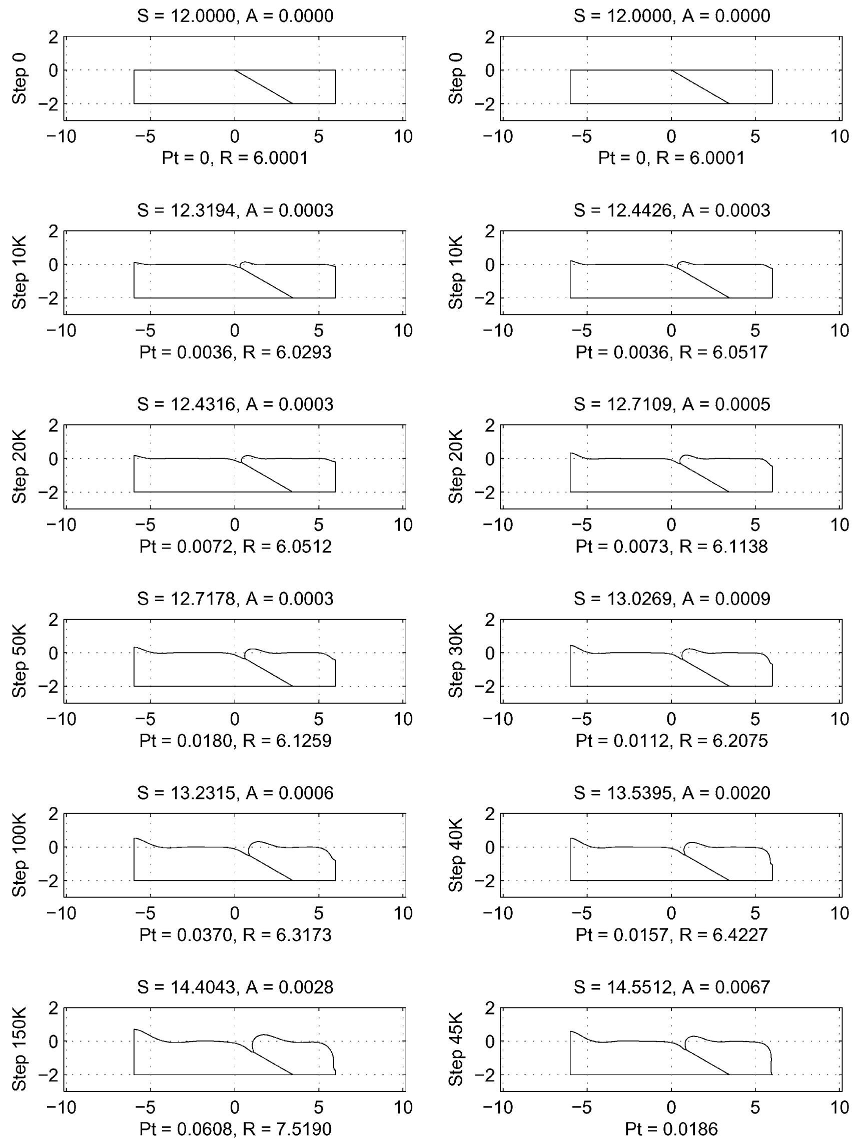

Fig. 24. Two-grain problem with a highly negatively tilted intergranular boundary in a weak and moderate electric field: $\alpha = 10$, $\beta = 5\pi/6$ (left column) and $\alpha = 20$, $\beta = 5\pi/6$ (right column).

elimination procedure to solve the boundary element set. However, the direct solver cannot use the availability of the initial guess from the previous time step. Iterative methods use effectively such an input, and thus they can be recommended. Since the time step of the explicit scheme for the fourth-order PDEs is fairly small, the field may be updated periodically once per several time steps without significant loss of accuracy.

Numerical simulations were run for various initial configurations and various ratios between diffusion and field forces. We find that an irregularity in the form of a negative tilt yields a stable evolution, while a positive tilt may develop instabilities. The analysis also shows that the groove between two grains may

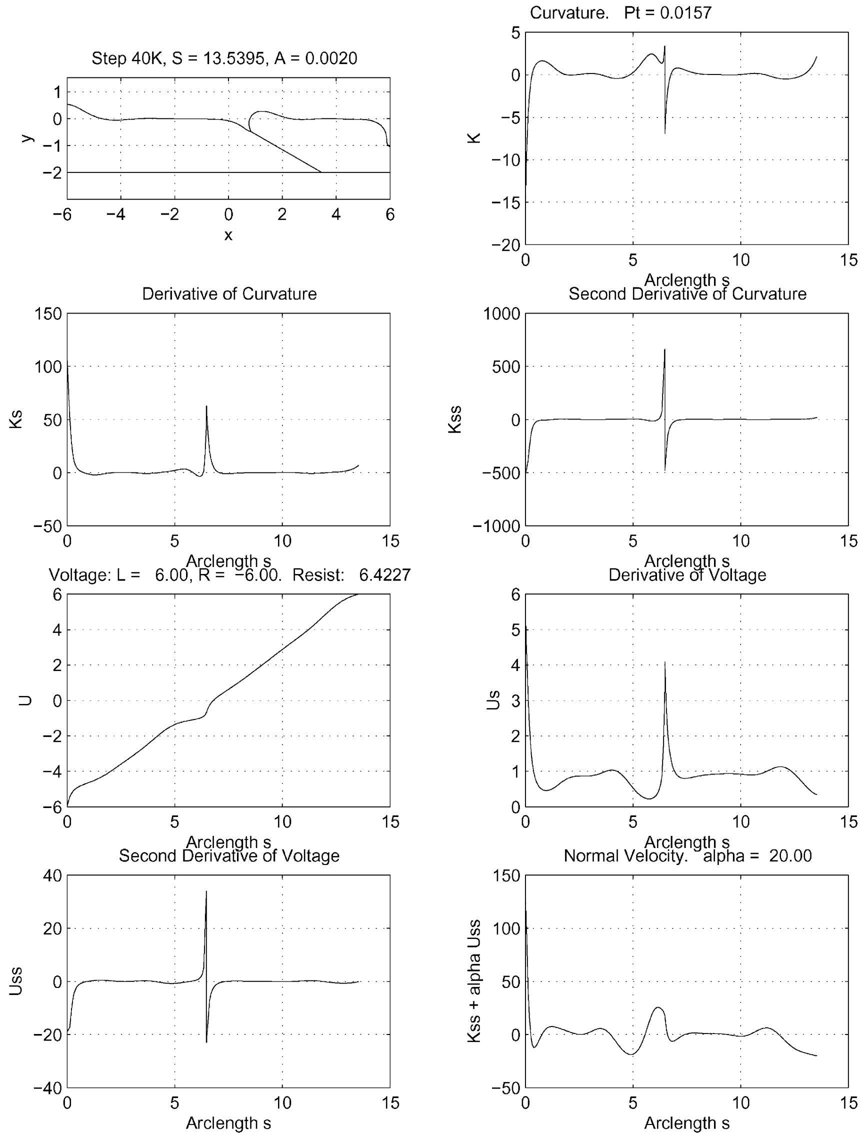

Fig. 25. Distribution of curvature and voltage after 10^5 steps for a large negative tilt of an intergranular boundary and a strong field: $\alpha = 20$ and $\beta = 5\pi/6$.

extend deeper under the single action of the surface diffusion forces than under the combined action of both diffusion and electric field.

References

[1] O. Kraft, E. Arzt, Numerical simulation of electromigration-induced shape changes of voids in bamboo lines, Applied Physics Letters 66 (16) (1995) 2063–2065.

[2] L. Klinger, L. Levin, Morphological stability of a heterophase interface under electromigration conditions, Journal of Applied Physics 79 (9) (1996) 6834–6839.

[3] L.M. Klinger, X. Chu, W.W. Mullins, C.L. Bauer, Grain-boundary slit propagation in an electric field, Journal of Applied Physics 80 (12) (1996) 6670–6676.
[4] H.K. Zhao, T.F. Chan, B. Merriman, S. Osher, A variational level set approach to multiphase motion, Journal of Computational Physics 127 (1996) 179–195.
[5] J.A. Sethian, Level Set Methods. Evolving Interfaces in Geometry, Fluid Mechanics, Computer Vision and Materials Science, Cambridge University Press, Cambridge, 1996.
[6] F. Paris, J. Canas, Boundary Element Method. Fundamentals and Applications, Oxford Science Publications, 1997.
[7] A. Averbuch, M. Israeli, I. Ravve, I. Yavneh, Computation for electromigration in interconnects of microelectronic devices, Journal of Computational Physics 167 (2001) 316–371.
[8] A. Averbuch, M. Israeli, I. Ravve, Electromigration of intergranular voids in metal films for microelectronic interconnects, Journal of Computational Physics 186 (2003) 481–502.
[9] L. Xia, A.F. Bower, Z. Suo, C.F. Shih, A finite element analysis of the motion and evolution of voids due to strain and electromigration induced surface diffusion, Journal of the Mechanics and Physics of Solids 45 (9) (1997) 1473–1493.
[10] Y.W. Zhang, A.F. Bower, L. Xia, C.F. Shih, Three dimensional finite element analysis of the evolution of voids and thin films by strain and electromigration induced surface diffusion, Journal of the Mechanics and Physics of Solids 47 (1999) 1473–1493.
[11] Y.W. Zhang, A.F. Bower, Three dimensional simulations of island formation in a coherent strained epitaxial film, Thin Solid Films 357 (1999) 8–12.
[12] O. Kraft, M. Hommel, E. Arzt, X-ray diffraction as a tool to study the mechanical behavior of thin films, Materials Science and Engineering A 288 (2000) 209–216.
[13] M.R. Gungor, D. Maroudas, Theoretical analysis of electromigration-induced failure of metallic thin films due to transgranular void propagation, Journal of Applied Physics 85 (4) (1999) 2233–2246.
[14] M.R. Gungor, D. Maroudas, Modeling of electromechanically induced failure of passivated metallic thin films used in device interconnections, International Journal of Fracture 109 (2001) 47–68.
[15] M. Schimschak, J. Krug, Electromigration-driven shape evolution of two-dimensional voids, Journal of Applied Physics 87 (2) (2000) 695–703.
[16] M. Mahadevan, R.M. Bradley, J.M. Debierre, Simulations of an electromigration-induced edge instability in single-crystal metal lines, Europhysics Letters 45 (1999) 680–685.
[17] J.B. Collins, Diffuse interface model of diffusion-limited crystal growth, Physical Review B 31 (1985) 6119–6122.
[18] D.N. Bhate, A. Kumar, A.F. Bower, Diffuse interface model for electromigration and stress voiding, Journal of Applied Physics 87 (4) (2000) 1712–1721.
[19] J.W. Cahn, J.E. Hilliard, Free energy of a nonuniform system. I. Interfacial free energy, The Journal of Chemical Physics 28-2 (1958) 258–267.
[20] D.R. Fridline, A.F. Bower, Influence of anisotropic surface diffusivity on electromigration induced void migration and evolution, Journal of Applied Physics 85 (6) (1999) 3168–3174.
[21] O. Kraft, E. Arzt, Electromigration mechanisms in conductor lines: void shape changes and slit-like failure, Acta Materialia 45 (4) (1997) 1599–1611.
[22] R. Spolenak, O. Kraft, E. Arzt, Effects of alloying elements on electromigration, Microelectronics Reliability 38 (1998) 1015–1020.
[23] O. Kraft, E. Arzt, Current density and line width effects in electromigration: a new damage-based lifetime model, Acta Materialia 46 (11) (1998) 3733–3743.
[24] D. Maroudas, M.R. Gungor, Continuum and atomistic modeling of electromechanically-induced failure of ductile metallic thin films, Computational Materials Science 23 (2002) 242–249.
[25] D. Fridline, A. Bower, Numerical simulations on stress induced void evolution and growth in interconnects, Journal of Applied Physics 91 (4) (2002) 2380–2390.
[26] M.R. Gungor, D. Maroudas, L.J. Gray, Effects of mechanical stress on electromigration-driven transgranular void dynamics in passivated metallic thin films, Applied Physics Letters 73 (26) (1998) 3848–3850.
[27] M.R. Gungor, D. Maroudas, Electromigration-induced failure of metallic thin films due to transgranular void propagation, Applied Physics Letters 72 (26) (1998) 3452–3454.
[28] M. Schimschak, J. Krug, Electromigration-induced breakup of two-dimensional voids, Physical Review Letters 80 (8) (1998) 1674–1677.
[29] M. Schimschak, J. Krug, Surface electromigration as a moving boundary value problem, Physical Review Letters 78 (2) (1997) 278–281.
[30] M. Mahadevan, R.M. Bradley, Simulations and theory of electromigration-induced slit formation in unpassivated single-crystal metal lines, Physical Review B 59 (16) (1999) 11037–11046.
[31] D.N. Bhate, A.F. Bower, A. Kumar, A phase field model for failure in interconnect lines due to coupled diffusion mechanisms, Journal of the Mechanics and Physics for Solids 50 (2002) 2057–2083.
[32] M.R. Gungor, D. Maroudas, Current-induced non-linear dynamics of voids in metallic thin films: Morphological transition and surface wave propagation, Surface Science 461 (2000) L550–L556.

[33] M.R. Gungor, D. Maroudas, Nonhydrostatic stress effects on failure of passivated metallic thin films due to void surface electromigration, Surface Science 432 (1999) L604–L610.
[34] M.R. Gungor, D. Maroudas, Non-linear analysis of the morphological evolution of void surfaces in metallic thin films under surface electromigration conditions, Surface Science 415 (1998) L1055–L1060.
[35] L.J. Gray, D. Maroudas, M.N. Enmark, E.F. Azevedo, Approximate Green's functions in boundary integral analysis, Engineering Analysis with Boundary Elements 23 (1999) 267–274.
[36] Z. Suo, Evolving material structures of small feature sizes, International Journal of Solids and Structures 37 (2000) 367–378.
[37] Z. Suo, Stable state of interconnect under temperature change and electric current, Acta Materialia 46 (11) (1998) 3725–3732.
[38] H.H. Yu, Z. Suo, An axisymmetric model of pore-grain boundary separation, Journal of the Mechanics and Physics of Solids 47 (1999) 1131–1155.
[39] B. Sun, Z. Suo, C.F. Cocks, A global analysis of structural evolution in a row of grains, Journal of the Mechanics and Physics of Solids 44 (4) (1996) 559–581.
[40] B. Sun, Z. Suo, W. Yang, A finite element method for simulating interface motion – I. Migration of phase and grain boundaries, Acta Materialia 45 (5) (1997) 1907–1915.
[41] B. Sun, Z. Suo, A finite element method for simulating interface motion – II. Large shape change due to surface diffusion, Acta Materialia 45 (12) (1997) 4953–4962.
[42] D. Adalsteinsson, J.A. Sethian, A level set approach to a unified model for etching, deposition and lithography I: algorithms and two-dimensional simulations, Journal of Computational Physics 120 (1995) 128–144.
[43] D. Adalsteinsson, J.A. Sethian, A level set approach to a unified model for etching, deposition and lithography II: three-dimensional simulations, Journal of Computational Physics 122 (1995) 348–366.
[44] J.A. Sethian, D. Adalsteinsson, An overview of level set methods for etching, deposition, and lithography development, IEEE Transactions on Semiconductor Manufacturing 10 (1) (1997) 167–184.
[45] H. Zhao, T. Chan, B. Merriman, S. Osher, A variational level set approach to multiphase motion, Journal of Computational Physics 127 (1996) 179–195.
[46] W.W. Mullins, Theory of thermal grooving, Journal of Applied Physics 28 (3) (1957) 333–339.
[47] W.W. Mullins, The effect of thermal grooving on grain boundary motion, Acta Metallurgic Materials 6 (6) (1958) 414–427.
[48] F.Y. Genin, W.W. Mullins, P. Wynblatt, The effect of stress on grain boundary grooving, Acta Metallurgic Materials 41 (12) (1993) 3541–3547.
[49] D. Maroudas, Dynamics of transgranular voids in metallic thin films under electromigration conditions, Applied Physics Letters 67 (6) (1995) 798–800.
[50] E. Artz, O. Kraft, W.D. Nix, J.E. Sanchez Jr., Electromigration failure by shape change of voids in bamboo lines, Journal of Applied Physics 76 (3) (1994) 1563–1571.
[51] J. d'Haen, J. Van Olmen, Z. Beelen, J.V. Manca, T. Martens, W. De Ceuninck, M. d'Olieslaeger, L. De Schepper, M. Cannaerts, K. Maex, In-situ SEM observations of electromigration in thin metal films at accelerated stress conditions, Microelectronics Reliability 40 (2000) 1407–1412.
[52] A.B. Amar, L.J. Cummings, G. Richardson, A theoretical treatment of void electromigration in the strip geometry, Computational Materials Science 17 (2000) 279–289.
[53] Y.X. Gao, H. Fan, Z. Xiao, A simulation of asymmetrical voids evolution induced by electromigration, Mechanics of Materials 32 (2000) 315–326.
[54] J.R. Rice, T.J. Chuang, Energy variations in difusive cavity growth, Journal of the American Ceramic Society 64 (1) (1981) 46–53.
[55] T.O. Ogurtani, E.E. Oren, Computer simulation of void growth dynamics under the action of electromigration and capillary forces in narrow thin interconnects, Journal of Applied Physics 90 (3) (2001) 1564–1572.
[56] E.E. Oren, T.O. Ogurtani, Void intergranual motion under the action of electromigration forces in thin film interconnects with bamboo structure, Materials Research Society Symposium Proceedings 695 (2002) 209–215.
[57] P. Huang, Z. Li, J. Sun, Finite element simulation of the diffusive growth of grain boundary voids, Modelling and Simulation in Materials Science and Engineering 8 (2000) 843–856.
[58] C.Y. Liu, S. Lee, T.J. Chuang, Grain boundary crack growth in interconnects with an electric current, Materials Science and Engineering B 86 (2001) 101–108.
[59] E. Liniger, L. Gignac, C.K. Hu, S. Kaldor, In situ study of void growth kinetics in electroplated Cu lines, Journal of Applied Physics 92 (4) (2002) 1803–1810.
[60] M. Nathan, E. Glickman, M. Khenner, A. Averbuch, M. Israeli, Electromigration drift velocity in Cu interconnects modeled with level set method, Applied Physics Letters 77 (21) (2000) 3355–3357.
[61] R.A. Augur, R.A. Wolters, W. Schmidt, A.G. Dirks, S. Kordic, Diffusion at the Al/Al oxide interface during electromigration in wide lines, Journal of Applied Physics 79 (6) (1996) 3003–3010.